Constrained Stochastic State Estimation of Deformable 1D Objects: Application to Single-view 3D Reconstruction of Catheters with Radio-opaque Markers

Raffaella Trivisonne, Erwan Kerrien, Stéphane Cotin

Constrained Stochastic State Estimation of Deformable 1D Objects: Application to Single-view 3D Reconstruction of Catheters with Radio-opaque Markers

Raffaella Trivisonne[a], Erwan Kerrien[b], Stéphane Cotin[a]

[a] *Université de Strasbourg, Inria, F-54000 Nancy, France*
[b] *Université de Lorraine, CNRS, Inria, LORIA, F-54000 Nancy, France*

Abstract

Minimally invasive fluoroscopy-based procedures are the gold standard for diagnosis and treatment of various pathologies of the cardiovascular system. This kind of procedures imply for the clinicians to infer the 3D shape of the device from 2D images, which is known to be an ill-posed problem.

In this paper we present a method to reconstruct the 3D shape of the interventional device, with the aim of improving the navigation. The method combines a physics-based simulation with non-linear Bayesian filter. Whereas the physics-based model provides a prediction of the shape of the device navigating within the blood vessels (taking into account non-linear interactions between the catheter and the surrounding anatomy), an Unscented Kalman Filter is used to correct the navigation model using 2D image features as external observations.
The proposed framework has been evaluated on both synthetic and real data, under different model parameterizations, filter parameters tuning and external observations data-sets.

Comparing the reconstructed 3D shape with a known ground truth, for the synthetic data-set, we obtained average values for 3D Hausdorff Distance of 0.81 ± 0.53 mm, for the 3D mean distance at the segment of 0.37 ± 0.17 mm and an average 3D tip error of 0.24 ± 0.13 mm . For the real data-set,we obtained an average 3D Hausdorff distance of 1.74 ± 0.77 mm, a average 3D mean distance at the distal segment of 0.91 ± 0.14 mm, an average 3D error on the tip of 0.53 ± 0.09 mm. These results show the ability of our method to retrieve the 3D shape of the device, under a variety of filter parameterizations and challenging conditions: uncertainties on model parameterization, ambiguous views and non-linear complex phenomena such as stick and slip motions.

Keywords: Constrained Unscented Kalman Filter, Physics-based simulation, Catheter Reconstruction, Endovascular Intervention, Computer Aided Surgery

1. Introduction and context

Image-guided minimally invasive procedures have become the gold standard for diagnosis or treatment of many pathologies. Whereas static images, such as CT or MRI scans, are rather

Email addresses: r.trivisonne@etu.unistra.fr (Raffaella Trivisonne), erwan.kerrien@inria.fr (Erwan Kerrien), stephane.cotin@inria.fr (Stéphane Cotin)

used for surgical planning or timely assessment of the surgical instrument position, real-time imaging, such as fluoroscopy, provides the visual feedback necessary for all interventional radiology procedures. The limitations of fluoroscopy based procedures are mainly associated with dose absorption and the intrinsic properties of X-rays images. Indeed, a contrast medium often needs to be injected in order to highlight anatomical structures, such as blood vessels. Fluoroscopic images are also affected by a lack of depth perception proper to all 2D projected images, which has been identified as one of the most important factors affecting clinical performance [1]. Augmenting the fluoroscopic image with a 3D overlay of the vessel surface [2] is a first step in restoring a 3D sense of the intervention site, and it was proved to improve the intervention outcome, reduce procedure time and facilitate navigation [3]. Recent approaches have leveraged deep learning techniques to recover the depth of a full field fluoroscopic image [4] but they fail to recover fine structures such as catheters except for very specific shapes [5]. In such cases 3D reconstruction is required. However, retrieving the 3D shape of an object from 2D features is an ill-posed problem: due to missing depth information, several 3D shapes may correspond to a given 2D configuration (Fig. 1). For endovascular interventions, one possible solution is to use bi-plane imaging systems in order to overcome the ambiguity of 2D images [6, 7, 8]. Contrary to what occurs with stereoscopic cameras in laparoscopic procedures, there is no risk of occlusion in fluoroscopic images. However, the wide baseline and the lack of texture makes image features extraction and matching more difficult. The accuracy of the reconstruction was reported in [8] as the mean distance (0.46mm) and error on the tip location (1.34mm). But such equipment is not very common in current practice. Given that single plane systems are more extensively used in clinical routine, in this work we propose a method to reconstruct, online and in 3D, the interventional device from 2D monocular fluoroscopic images. In this context, previous methods may

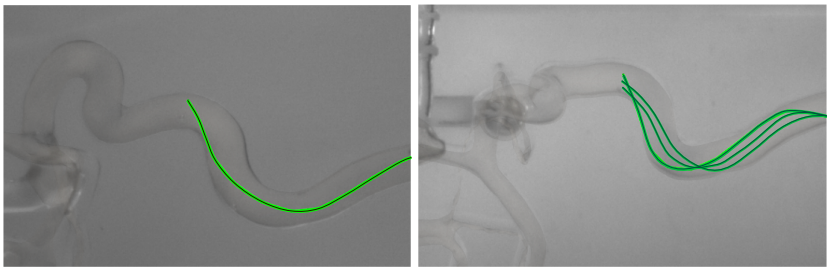

(a) Side view (b) Top view

Figure 1: **2D-3D Registration**. Ill-posed problem: several 3D shapes may correspond to the same 2D configuration. Catheter shapes can be seen as different in a top view (b) but may project onto the same curved line in a side view (a).

be classified as follows: reconstruction methods exploiting position or shape sensors, computer vision methods based on the use of images and geometric models, and reconstruction methods combining fluoroscopic images and a physics-based model of the device.

For the methods using external sensors, the general idea is to embed an external sensor into the instrument, in order to have a three-dimensional knowledge on the position of the tip or other parts of the device. Condino et al. [9] proposed to use electro-magnetic (EM) tracking in combination with occasional intra-operative CTA. Similarly, in [10] the EM data are completed with ultrasonography to update pre-operative CT data. However, image acquisition and registration are time consuming and cannot be performed frequently enough to guarantee consistency between the virtual and real anatomies. EM trackers were also combined in [11] with a robotic

catheterization system, providing a 3D instrument position and orientation visualization instead of the classic 2D fluoroscopic view. Although embedded trackers can give a rather precise location of the catheter, they allow only for a very partial reconstruction of the device and a full shape cannot be retrieved. As an example close to our work [12] placed 5 EM sensors along a cardiac ablation catheter to retrieve its position in combination with (simulated) fluoroscopic images. They report a root mean square (RMS) median error of 3.7 mm, with already 1.81 mm of error in the EM to image registration process. In addition, embedding EM sensors on the interventional device implies significant changes on the clinical workflow and restricts clinical applications. EM Localization errors may further increase in the clinical environment of an operating room, where interactions with ferromagnetic materials cannot be neglected [13].

Computer vision methods aim at retrieving the 3D reconstruction of objects from 2D images. Given the illposedness of the problem, some hypotheses need to be made in order to restrict the space of possible solutions. In the case of an interventional device, it is assumed to lay inside the vessel surface and regularization constraints are applied to the geometric model and its deformations. Authors in [14], propose to constrain the reconstructed catheter to match the vessel centerline. Such regularization criteria lead to shapes that do not perfectly match reality. In particular, aligning with the centerline precludes from reproducing any contacts between the device and the vessel surface, whereas they occur very frequently, especially in curved vessels. In [15] 3D device reconstruction is defined as a smooth curve that both lies within the blood vessels and projects on the guidewire segmented in the images. The curve smoothness and continuity are ensured with a set of priors, including here again a constraint to stay close to the vessel centerline. Ambiguous cases are not handled and left for the clinician to interpret. Using a particle filter, Brückner et al. [16] combines the 3D geometric model of the vessels with the back-projection of 2D features, creating a 3D probability distribution of the wire positions which is recursively propagated. A spline shape model with maximum length and minimum curvature are priors set to regularize the maximum a posteriori solution. A probabilistic framework is also used in [17] to track the device tip in 3D, using the closest point on the vessel surface as a geometric prior.

All these reconstruction methods rely on geometric prior models of the shape of the catheter and cannot guarantee a reliable reconstruction, in particular under ambiguous views. Moreover the device motion is not modeled, which can make 2D-3D data association, and thereafter reconstruction fail, especially after sudden modifications of the catheter's shape (e.g. following a contact with the surrounding anatomy). Errors of 1.5 mm for the mean distance and around 2 to 3 mm for the tip localization are typically reported.

More sophisticated modeling of the device, like a physics based approach, could provide a better description and overcome the above limitations. In [18] we proposed a constrained shape-from-template method combining a physics-based model of the catheter with 2D image features through a constrained approach using Lagrange multipliers. No interactions with the surrounding anatomy were taken into account during the navigation of the catheter, whereas device motion was entirely driven by the detected image features. Device reconstruction was demonstrated in simple cases but not under ambiguous scenarios, such as anatomy occlusions or partial views. In addition, uncertainties on mechanical characterization of the device, as well as noise on external observations were taken into account only through empirical parameters.

Given the aforementioned approaches, multiple sources of information need to be combined to retrieve a reliable reconstruction of the device: a shape model (physics-based or geometric, taking into account motion and deformation), a navigation model, including forces modeling the insertion of the device and contacts with the surrounding anatomy, and information on the current state of the device (projective 2D from image features, 3D from position or shape sensors). All

of the above are prone to be tainted with errors. Recursive Bayesian estimation methods have been investigated to handle those various sources of error. They allow to retrieve the most likely state of a system, described by a process model and observed through external measurements, potentially affected by noise. In [19], a catheter insertion model is combined with 3D positions measured by external EM sensors through an Extended Kalman Filter (EKF). The filter enables to manage both noisy measurements of EM trackers and potential inaccuracies of the catheter insertion model. In a more general computer vision context, sensor-less methods have been proposed to recover the 3D shape of a deforming non-rigid object from a monocular sequence. In particular Finite Element (FE) models enable to implement sophisticated priors on the shape to capture realistic deformations while being robust to occlusions [20],[21],[22],[23]. It has been recently shown how a FE model could be leveraged in an EKF framework to achieve online reconstruction [24],[25]. Two hypotheses are necessary for this method: they assume to know the deformation modes of the surface and they suppose to detect and track some to 2D features, whose correspondences with 3D points of the FE model are assumed to be known. The FE model, driven by the 2D detected features, capture elastic deformations of the surface but it does not provide any information about the dynamic behavior of the object; contacts and collision are not taken into account, whereas only fixed physical constraints can be included in the model. In addition, such framework could not directly fit our specific problem of catheter reconstruction, as a surface FE model cannot be applied to a curved shape like the interventional device.

2. Method

The main aim of our work is to reconstruct the 3D shape of the interventional device from 2D single-view fluoroscopic images. To this end, we propose a finite element (FE) model reproducing the navigation within blood vessels through a constrained physics-based simulation. Contrary to existing methods, our model aims at having a better prediction of the device physical behavior, in particular taking into account contacts with the surrounding blood vessels. Through a Bayesian filter, the predicted shape is corrected with 2D observations of the current real shape, detected and tracked in an image sequence. Such stochastic formulation allows not only to take into account inaccuracies in the navigation model (mechanical characterization of the catheter model, uncertainties on applied constraints, etc), but it also allows to take into account the missing depth information of 2D image features as a further source of uncertainty of the stochastic state.

Given the non-linearity of both the model and the observations, we propose to use an Unscented Kalman Filter [26]. One of the major contributions of this work is a solution to the constrained state estimation problem raised by contacts. In stochastics, a constrained estimation occurs when not all the values of the random variable are acceptable samples. In our case, as the device is constrained to stay inside the vessel, the estimated positions cannot assume all the possible values within their probability distribution (e.g. outside the vessel surface). The proposed method casts such constrained estimation as a Non-linear Complementarity Problem (NLCP) solved using a Gauss-Seidel Method.

Several approaches are combined in this work. In this section, we first introduce some generic background about Bayesian filtering. Then, we present the physics based model of the catheter navigation with its dynamics equations. The end of the section describes the whole proposed formalism where both concepts are combined.

2.1. *Bayesian Filtering*

Bayes filters recursively estimate the probability density function describing the random state of a system. In the discrete domain, such state can be represented as a random variable X_k, with k being the discrete time-step, assumed to evolve according to a process model. The process model can be expressed as a collection of known functions $g_k(\cdot)$ such that:

$$\boldsymbol{X}_k = g_k(\boldsymbol{X}_{k-1}, \nu_k) \tag{1}$$

Other external data may also be available at each time-step providing potentially partial observations $\boldsymbol{Z}_k$ of the current state of the system. Such observations are related to the state through to known observation functions $h_k(\cdot)$:

$$\boldsymbol{Z}_k = h_k(\boldsymbol{X}_k, \omega_k) \tag{2}$$

Both state and observations are affected by random noise processes, respectively ν_k and ω_k. Bayes filters are based on a general prediction-update scheme of the posterior probability $P(\boldsymbol{X}_k|\boldsymbol{Z}_k)$. Given the previous estimation $P(\boldsymbol{X}_{k-1}|\ \boldsymbol{Z}_{k-1})$ at time $k-1$, the first step consists of computing a prediction of the probability density function by propagation through the process model g_k: $P(\boldsymbol{X}_k|\boldsymbol{Z}_{k-1})$. Then, the predicted estimate is updated using the current observation, to provide the posterior estimate: $P(\boldsymbol{X}_k|\boldsymbol{Z}_k)$. The final state of the system $\boldsymbol{X}_k$ is thereafter selected according to some optimality criterion (e.g. Maximum A Posteriori or expected value).

Kalman filters [27] are a particular case of Bayes filters where noise processes are assumed to be Gaussian and both process and observation models are linear and can be expressed by matrices $\mathbf{G}_k$ and $\mathbf{H}_k$:

$$\begin{aligned} \boldsymbol{X}_k &= \mathbf{G}_k\boldsymbol{X}_{k-1} + \boldsymbol{\nu}_k, \quad \text{with} \quad \boldsymbol{\nu}_k = \mathcal{N}(0, \boldsymbol{Q}_k) \\ \boldsymbol{Z}_k &= \mathbf{H}_k\boldsymbol{X}_k + \boldsymbol{\omega}_k, \quad \text{with} \quad \boldsymbol{\omega}_k = \mathcal{N}(0, \boldsymbol{R}_k) \end{aligned} \tag{3}$$

Whenever these assumptions are not possible, the Kalman filter formalism may still be used, but some approximations are necessary. For example, the Extended Kalman Filter (EKF) handles non-linear process and observation models, and propagates the system covariance thanks to their first order approximations: $\mathbf{G}_k$ and $\mathbf{H}_k$ are the Jacobian matrices of g_k and h_k [28]. In this work, we decided to use an Unscented Kalman Filter (UKF) [26, 28] that applies a sampling based approach to handle non-linear prediction and observation models (eq.((1)-(2))). The idea behind a UKF is to draw r samples from the current estimate of the posterior probability in such a way that these samples, called *sigma-points*, capture the first two moments of the posterior distribution, with minimum distortion on the third moment [26]. Each sigma-point σ_j is propagated through the non-linear process, then observation models, which enables to compute the transformed mean and covariance of the state.

In our context, the boundary condition represented by the vessel wall and the non-rigid contacts which occurring between the device and the surrounding surface are non-linear phenomena, varying through time, which lead to discontinuities in velocities of the objects in contact. The by-design preservation of the first moments of the probability density function makes UKF a better choice than EKF such kind of non-linearities occur [26, 29]. In addition, the implementation of an EKF, where the computation of derivatives of both the state transition and the observation matrix is needed, is not straightforward nor computationally efficient in our context of collision response and projective observations. The following table summarizes the notations used throughout the paper:

Table 1: **Notations : discrete time index k was dropped for simplicity**

$\boldsymbol{X}$ state vector	$\boldsymbol{P}$ model covariance
$\boldsymbol{\sigma}_j$ j^{th} sigma-points	$\mathbf{I}^{(j)}$ unit vector to generate $\boldsymbol{\sigma}_j$
$\boldsymbol{Q}$ model noise covariance matrix	$\mathbf{Z}$ observations vector
$\boldsymbol{P}^{\bar{Z}}$ observations covariance	$\boldsymbol{R}$ obs. noise covariance matrix
$\boldsymbol{P}^{\bar{X}\bar{Z}}$ state-observations cross-covariance	$\boldsymbol{K}$ Kalman gain
g prediction function	h observation function

2.2. *Catheter Navigation Model*

Catheters are flexible but inextensible slender non-linear elastic objects. A vast number of methods have been developed to model the mechanical behavior of such objects, up to state-of-the-art approaches that can now handle large elastic deformation and complex contacts with the surrounding vessels in a fast and stable way [30]. In this paper, we use a physics-based model based on beam theory [31], solved using an efficient co-rotational finite element (FE) approach [32]. Our model is represented as a series of N serially-linked beam elements, where each node has 6 Degrees of Freedom (DoFs) [33] (see Fig. 2.a). To simulate the navigation of the device inside the anatomy, we directly apply a constant force to the last node of the catheter, mimicking the surgical gesture of insertion within the blood vessel, while being constrained inside the surface (see Fig. 2.b) .

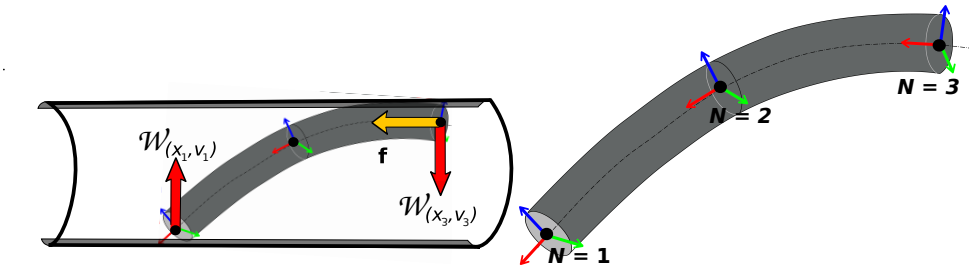

(a) (b)

Figure 2: **FE Physics-Based Model**. (a) Lateral view of the simulated device inside the surface. Yellow arrow represent the insertion force $\mathbf{f}$, directly applied to the last node, and spread to the other nodes of the FE model according to the mechanical properties of the object. Such force produces catheter forward motion; red arrows are the surface constraint forces $\mathcal{W}(\mathbf{x}_i, \mathbf{v}_i)$ applied on the i^{th} node whenever a contact occurs. (b) The device is modeled as a series of N connected 6 DoFs beams

Co-rotational FE formulation, it is a trade-off between accuracy and computation time. In general, two factors have to be taken into account in order to define an efficient model of a catheter-like device: the different motions the device can undergo and the resulting deformations and interactions with surrounding objects. We show, in Sec. 3.2.4, that the co-rotational FE model properly describes the dynamic behaviour of the catheter, while allowing to take into account non-linear contacts between objects.

2.2.1. *Dynamics of Deformable Model and Implicit Integration*

The dynamics of the interventional device can be generally described by Newton's second law of motion: $\mathbb{M}(\mathbf{x})\ddot{\mathbf{x}} = \mathbb{F}(t) - f(\mathbf{x}, \dot{\mathbf{x}}) + \mathcal{W}(\mathbf{x}, \dot{\mathbf{x}})$ (here expressed as second order differential equation). Where $(\mathbf{x}, \dot{\mathbf{x}}, \ddot{\mathbf{x}})$ (each $\in \mathbb{R}^N$ with N being the number of nodes of the FE model) express

respectively position, velocity and acceleration of a catheter's node; $\mathbb{M}(\mathbf{x})$ and $f(\mathbf{x}, \dot{\mathbf{x}})$ represent respectively the inertia matrix and the internal forces, both derived from the co-rotational FE model and $\mathbb{F}(t)$ expresses the external forces while $\mathcal{W}(\mathbf{x}, \dot{\mathbf{x}})$ formalizes the boundary conditions applied to the model.

In case of interventional device navigation, such boundary conditions are represented by the vessel wall and the contacts that occur with the device. Non-rigid contacts are non-linear phenomena, varying through time, and collision response on mechanical objects leads to discontinuities in velocities. This problem belongs to the domain of non-smooth mechanics, for which accelerations are not defined. To handle non-smooth dynamics while enabling fast computations, we use a *time-stepping* method [34] based on an Implicit Integration scheme.

The discrete variables are then expressed as $\mathbf{x} = \mathbf{x}(t)$, $\mathbf{v} = \dot{\mathbf{x}}(t)$ with the respective differences $\mathbf{\Delta x} = \mathbf{x}(t + T) - \mathbf{x}(t)$ and $\mathbf{\Delta v} = \mathbf{v}(t + T)$ - $\mathbf{v}(t)$ (T is the time-step). Non-linear terms, such as $f(\mathbf{x}, \dot{\mathbf{x}})$, are linearized using a first order Taylor series expansion. Such linearization corresponds to the first iteration of Newton-Raphson algorithm. Limited Newton-Raphson iterations enable faster computations, with the risk of not obtaining full convergence of the solution. In our scenario, given the hypothesis of small displacements, a single iteration is usually sufficient to provide a reliable solution.

The implicit velocity update is then computed as: $(\mathbf{M} - T\frac{\partial f}{\partial \mathbf{v}} - T^2\frac{\partial f}{\partial \mathbf{x}})\mathbf{\Delta v} = T(\mathbf{f} + T\frac{\partial f}{\partial \mathbf{x}}\mathbf{v}) + T\mathbf{J}^T\boldsymbol{\lambda}$ After discretization, the matrix $\mathbf{M}$ expresses the mass and it can be considered as constant and lumped; in particular we obtain a diagonal matrix $\mathbf{M} \in \mathbb{R}^{12N\times 12N}$. The partial derivatives of elastic forces can be defined as $\mathbf{K} = \frac{\partial f}{\partial \mathbf{x}}$ and $\mathbf{B} = \frac{\partial f}{\partial \mathbf{v}}$, respectively approximating the stiffness of all the vertices ($\mathbf{K} \in \mathbb{R}^{12N\times 12N}$) and damping of the model ($\mathbf{B} = \alpha\mathbf{M} + \beta\mathbf{K}$). The term $\mathbf{J}^T\boldsymbol{\lambda}$ expresses the linearized contacts. A more detailed explanation will be provided in following sections. Last equation, rewritten as a linear system, becomes:

$$\underbrace{(\mathbf{M} - T\mathbf{B} - T^2\mathbf{K})}_{\mathbf{A}}\mathbf{\Delta v} = \underbrace{T(\mathbf{f} + T\mathbf{K}\mathbf{v})}_{\mathbf{b}} + T\mathbf{J}^T\boldsymbol{\lambda} \tag{4}$$

Matrices $\mathbf{M}, \mathbf{B}, \mathbf{K}$ are computed by summing up the contributions of each element to its vertices. This operation is called the assembly and for elastic deformations, matrix $\mathbf{A} \in \mathbb{R}^{12N\times 12N}$ is symmetric definite positive. The vector $\mathbf{b} \in \mathbb{R}^{12N}$ expresses applied external forces.

2.2.2. Contact Constraints

As stated above, the interventional device is forced to remain within the blood vessels through boundary constraints expressed as non-linear inequalities. Regardless of the method used to integrate boundary conditions, the first step is to detect potential contacts. In our case, potential points in contact are identified through a proximity detection between catheter nodes and the vessel partitioned surface (for details see [35, 36]). This basically consists of identifying, for each node of the catheter, the closest point on the surface. We define the interior normal $\mathbf{n}$ to the surface at that point. Then, all the identified contact directions are gathered in matrix $\mathbf{J}$. In particular, the transpose of the Jacobian $\mathbf{J}^T = \frac{\partial \mathcal{W}}{\partial \mathbf{x}}$, represent the linearization of the applied constraints.

Once proximity detection has been performed, we must verify whether contact has occurred or not. Collision response is performed based on Signorini's law:

$$\begin{cases} \boldsymbol{\delta}_\mathbf{n} \geq 0 \\ \boldsymbol{\lambda}_\mathbf{n} \geq 0 \\ \boldsymbol{\delta}_\mathbf{n} \cdot \boldsymbol{\lambda}_\mathbf{n} = 0 \end{cases} \tag{5}$$

where $\delta_{\mathbf{n}}$ represents the interpenetration which must be ensured non negative ($\boldsymbol{\delta}_{\mathbf{n}} \geq 0$). If interpenetration has occurred (i.e. $\boldsymbol{\delta}_{\mathbf{n}} \leq 0$ and the point falls outside the boundary condition) a contact force $\boldsymbol{\lambda}_{\mathbf{n}}$ must be applied to correct the violation of the constraint. For each point, contact forces are applied along the respective direction, gathered in $\mathbf{J}^T$.

Friction phenomena are taken into account according to Coulomb's friction law. A component of the contact forces will hence depend on a friction parameter μ:

$$\boldsymbol{\lambda}_{\mathbf{T}} = -\mu \|\boldsymbol{\lambda}_{\mathbf{n}}\| \frac{\delta_{\mathbf{T}}}{\|\delta_{\mathbf{T}}\|} \tag{6}$$

2.2.3. Constraint-based Solution

In order to integrate the dynamics of the non-rigid objects (Eq. (4)), with contact's law and friction's law (Equations (5)-(6)), we use a Lagrange multiplier approach with a single linearization per time-step. Penalty methods, such as spring-like forces, which try to keep the object inside the surface (i.e. enforcing the boundary conditions) are not suitable nor stable solutions for our problem. Instead, we introduce Lagrange multipliers ensuring that at the end of each time step we have a valid configuration (every point of the catheter lies inside the vessel) while reducing the computational cost.

Based on eq. (4), the behaviour of two interacting objects may be described as a Karush-Kuhn-Tucker system (KKT) as follows:

$$\begin{cases} \mathbf{A}\boldsymbol{\Delta}\mathbf{v} = \mathbf{b} + \mathbf{J}^T\boldsymbol{\lambda} \\ \mathbf{J}^T\boldsymbol{\Delta}\mathbf{v} = \boldsymbol{\delta} \end{cases} \tag{7}$$

The aim is to compute $\boldsymbol{\lambda}$ deriving from contact's law. Such resolution is performed through iterative steps:

1. **Free Motion**: we solve the linear system $\mathbf{A}\boldsymbol{\Delta}\mathbf{v} = \mathbf{b}$, which will provide $\boldsymbol{\Delta}\mathbf{v}^{free}$ at the end of the time step, as if no interaction constraints where applied ($\boldsymbol{\lambda} = 0$ in eq.(4)).

2. **Constraint definition**: we perform proximity detection (as described in sec. 2.2.2) in order to linearize the constraint by computing the Jacobian of the constraints $\mathbf{J}$. The collision detection is performed using the positions at the beginning of the time step.

3. **Compliance Computation**: Once both the directions of constraints, expressed in $\mathbf{J}$, and the free motion $\boldsymbol{\Delta}\mathbf{v}^{free}$ (without constraints) are known, we can define $\boldsymbol{\delta}$, being the violation of the constraint. In practice, it is the distance the interpenetration, projected along the constraint directions. From Eq.(4): $\boldsymbol{\Delta}\mathbf{v} = \boldsymbol{\Delta}\mathbf{v}^{free} - \mathbf{A}^{-1}\mathbf{J}^T\boldsymbol{\lambda}$, we can rewrite the second term of Eq. (7) as:

$$\underbrace{(\mathbf{J}\mathbf{A}^{-1}\mathbf{J}^T)}_{\mathbf{W}}\boldsymbol{\lambda} = \mathbf{J}\boldsymbol{\Delta}\mathbf{v}^{free} - \boldsymbol{\delta} \tag{8}$$

   The *Delassus Operator* $\mathbf{W}$ represents the mechanical coupling between the constraints and it is the most expensive step of the simulation as it requires to explicitly multiply the inverse of the mechanical matrix $\mathbf{A}$ with the Jacobian of the contacts.

4. **Constraint Resolution**: The above expression provides a Non-linear Complementarity Problem (NLCP) where there are two unknowns: the applied forces $\boldsymbol{\lambda}$ and the violation $\boldsymbol{\delta}$. This is solved through an iterative Gauss-Seidel Method, where each constraint is treated singularly independently from other current constraints. For more details on this step see:[35] and [36]).

5. **Final Correction**: Once contact forces $\boldsymbol{\lambda}$ are known, it is possible to compute the final position and velocity of each node of the model:

$$\begin{aligned} \boldsymbol{\Delta}\mathbf{v} &= \boldsymbol{\Delta}\mathbf{v}^{free} - \mathbf{A}^{-1}\mathbf{J}^T\boldsymbol{\lambda} \\ \mathbf{v}_T &= \mathbf{v} + \boldsymbol{\Delta}\mathbf{v} \\ \mathbf{x}_T &= \mathbf{x} + T\mathbf{v}_T \end{aligned} \tag{9}$$

2.3. *Image Feature Observations*

The projected shape of the catheter should be detected in fluoroscopic images. Several solutions have been proposed to detect and track a curve in an image sequence [37, 38, 39]. We made the assumption extensively used in monocular reconstruction to detect and track 2D features corresponding to known 3D points. In practice, the catheter is assumed to be tagged with M radio-opaque markers $\{P_i = (x_i, y_i, z_i)\}_{i\in[1,M]}$, equally distributed along the catheter length. Each marker P_i is thus related to the catheter nodes through a constant linear mapping $\mathcal{M}_i$ (see Fig. 3). In the image, each marker is detected at pixel coordinates $q_i = (u_i, v_i)$ which are related to the 3D marker coordinates through the $[3 \times 4]$ projection matrix $\mathbf{C}$, such that

$$\underline{\mathrm{q}}_i = \mathbf{C}\,\underline{\mathrm{P}}_i \tag{10}$$

where the underline notation expresses homogeneous coordinates. $\mathbf{C}$ only depends on the X-ray view incidence, which is assumed constant during the acquisition of a fluoroscopic sequence. This matrix can be accurately estimated from the view parameters (angles, source-to-image distance, ...) with a calibrated vascular C-arm [2]. We assume 2D-3D correspondences, between detected image-features and the FE model, to be known.

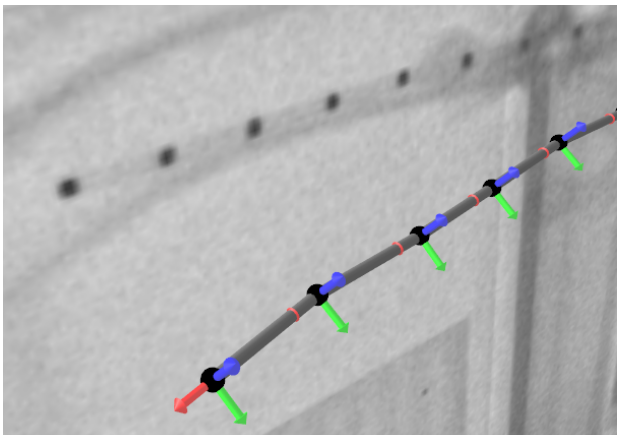

Figure 3: **Image Feature Detection**. Radio-opaque markers are related to 6 DoF catheter's nodes (black spheres) through a known constant mapping $\{P_i = \mathcal{M}_i(\mathbf{x})\}$. Without loss of generality, we suppose markers to exactly match the nodes.

2.4. *Combined Framework*

We propose to combine the physics-based model with external 2D observations through a Bayesian filter. The use of the filter allows to retrieve an accurate 3D shape taking into account

the uncertainty on both the model and the external measurements. In the following notation, the index i specifies the catheters nodes, k indicates the discrete time-step, and j refers to sigma-points.

2.4.1. State Vector

Usually, in Bayesian Filter for trajectory estimation, the state vector is composed of position, velocity and acceleration of the object [26]. In our case, we estimate the positions and velocities of each catheter node given that, using the time integration scheme presented in Eq. (4), the acceleration is in fact expressed as a difference of velocities. Considering the i^{th} node, the state vector can hence be expressed as:

$$\boldsymbol{X}(i) = [\underbrace{x_i, y_i, z_i, \psi_i, \theta_i, \phi_i}_{\textbf{position } \mathbf{x}_i^t}, \underbrace{v_{x_i}, v_{y_i}, v_{z_i}, v_{\psi_i}, v_{\theta_i}, v_{\phi_i}}_{\textbf{velocity } \mathbf{v}_i^t}] \tag{11}$$

with $i \in (1, N)$ and N being the number of serially linked beams. Given that position and velocity are expressed taking into account 6DoFs, the whole state will be $\boldsymbol{X} \in \mathbb{R}^{12N}$.

2.4.2. Prediction Model

At time k, the temporal evolution of the state results from a two step process: first solve Eq. (7) for $\boldsymbol{\Delta}\mathbf{v}_k$ and then update the positions $\mathbf{x}_k$ and velocities $\mathbf{v}_k$ through Eq. (9).

The noise on this process mainly comes from an uncertain characterization of the FE model, that it is propagated to the estimated $\boldsymbol{\Delta}\mathbf{v}$, solution of Eq. (7). The resultant noise is modeled as a Gaussian additive random term ν_k. As a result, our process model is given by

$$\begin{aligned}
\mathbf{A}_k \boldsymbol{\Delta}\mathbf{v}_k &= \mathbf{b}_k + \mathbf{J}_k^T \boldsymbol{\lambda}_k \\
\mathbf{J}_k^T \boldsymbol{\Delta}\mathbf{v}_k &= \boldsymbol{\delta}_k && (12)\\
\boldsymbol{\Delta}\hat{\mathbf{v}}_k &= \boldsymbol{\Delta}\mathbf{v}_k + \nu_k && (13)\\
\mathbf{v}_k &= \mathbf{v}_{k-1} + \boldsymbol{\Delta}\hat{\mathbf{v}}_k \\
\mathbf{x}_k &= \mathbf{x}_{k-1} + T\mathbf{v}_k && (14)
\end{aligned}$$

Eqs. (12) provide $\boldsymbol{\Delta}\mathbf{v}_k$, that is disturbed by random noise ν_k in (13). The velocity $\mathbf{v}_k$ and the position $\mathbf{x}_k$ are then updated in Eq. and (14). We assume an independent and constant noise so that $E[\nu_k(\nu_k)^t] = \sigma_{mod}\mathbf{I}_{6N}$.

This results in the state covariance matrix expressed as:

$$\boldsymbol{Q} = \mathbf{I}_N \otimes \begin{pmatrix} \mathbf{0}_{6\times6} & \mathbf{0}_{6\times6} \\ \mathbf{0}_{6\times6} & \sigma_{mod}^2 \mathbf{I}_6 \end{pmatrix} \tag{15}$$

and an initial state covariance matrix, which expresses the uncertianty on the initial configuration, expressed as:

$$\boldsymbol{P}_0 = \mathbf{I}_N \otimes \begin{pmatrix} \sigma_{\mathbf{x}_{mod}}^2 \mathbf{I}_6 & \mathbf{0}_{6\times6} \\ \mathbf{0}_{6\times6} & \sigma_{\mathbf{v}_{mod}}^2 \mathbf{I}_6 \end{pmatrix} \tag{16}$$

where $\otimes$ is the Kronecker product and $\mathbf{I}_N$ is the $N \times N$ identity matrix.

2.4.3. Observation Model

Observations are the projection of the radio-opaque markers, detected in the images:

$$\boldsymbol{Z}(i) = q_i = [u_i, v_i]^t \qquad \forall i \in [1, M] \tag{17}$$

According to our observation model, the i^{th} detected feature will depend on the corresponding 3D marker, through the calibrated projection matrix $\mathbf{C}$:

$$\underline{\boldsymbol{Z}}(i) = \mathbf{C}\,[x_i, y_i, z_i, 1]^t = \begin{pmatrix}\mathbf{U} & \mathbf{0}_{3\times 9} & \mathbf{V}\end{pmatrix} \begin{bmatrix}\mathbf{X}(i) \\ 1\end{bmatrix} = \mathbf{C}_+\,\underline{\mathbf{X}}(i) \tag{18}$$

where $\mathbf{U}$ and $\mathbf{V}$ are respectively a 3×3 matrix and a 3-vector such that $\mathbf{C} = (\mathbf{U}\,\mathbf{V})$. The observation function $h_k(\cdot)$ is therefore constant : $h_k = h$. For the sake of simplicity, we assumed here that identity mappings relate markers to nodes such that a node is defined at each marker location, such that M, the number of markers, equals N, the number of nodes.

The observation vector $\boldsymbol{Z}_k \in \mathbb{R}^{2N}$ concatenates the locations of all the 2D markers detected in the image at time k. We assume that all observations are independent and that the noise ω on the observations does not depend on the acquisition time. Therefore, its covariance matrix is constant and diagonal: $\boldsymbol{R} = \sigma^2_{obs}\mathbf{I}_{2N}$.

2.4.4. Filter Workflow and Computation Time

The *simplex method* [29] was used to generate the r sigma-points with a minimum computation cost: it requires only $r = p + 1$ sigma-points, where $p = 12N$ is the state vector size. A generic sigma-points is expressed as

$$\boldsymbol{\sigma}_j = [\boldsymbol{\sigma}_{\mathbf{x}_1}, \boldsymbol{\sigma}_{\mathbf{v}_1}, \cdots, \boldsymbol{\sigma}_{\mathbf{x}_N}, \boldsymbol{\sigma}_{\mathbf{v}_N}]^t_j \quad \text{with} \;\; j \in [1, r] \tag{19}$$

Alg.(1) summarizes an UKF estimation, modified to take into account our specific process and observation model. Fig. 4 summarizes the global pipeline in which filter and simulation are combined. In the prediction phase, an entire simulation step is run for every sigma-point $\boldsymbol{\sigma}_j$. From each propagated $\hat{\boldsymbol{\sigma}}_j$ we can compute the predicted observations $\hat{\boldsymbol{Z}}_j$, through the observation function $h(\cdot)$. A major challenge of our method lies in achieving high computation time. Whereas a classic physics-based constrained simulation may be performed in real-time (over 25 FPS), such combined approach entails higher computation times due to the multiple simulations performed during each time-step. In order to optimize computation time, one possible solution is to reduce the state vector size by not taking into account all the degrees of freedom of the mechanical model. Results reported in Section 3.5 were obtained with a reduced state vector where the orientations were removed: $\boldsymbol{X}(i) = [x_i, y_i, z_i, v_{x_i}, v_{y_i}, v_{z_i}, v_{\psi_i}, v_{\theta_i}, v_{\phi_i}]$. In the process, the orientations $(\psi_i, \theta_i, \phi_i)$ were mathematically computed from the estimated positions (x_i, y_i, z_i).

2.4.5. Constrained State Estimation

The catheter bounded within the vessel surface represents, from the filter point of view, a problem known as Constrained State Estimation [40]. During the prediction phase, random sampling of the Gaussian distribution may generate some sigma-points $\boldsymbol{\sigma}_j$ whose positions fall outside the vessel surface (Fig. 5(b)), representing configurations not physically coherent.

Initialization: set X_0, P_0, Q, R
for *each simulation step k* **do**
  Prediction:
  for $j = 1 : r$ *with r = number of sigma-points* **do**
    generate sigma-points
    $[\sigma_{\mathbf{x}}, \sigma_{\mathbf{v}}]_{j_k} = [\mathbf{x}_{k-1}, \mathbf{v}_{k-1}] + \sqrt{P}_{k-1}\mathbf{I}^{(j)}$
    propagate sigma-points (eqs. (12)- (14)*)*
    $\mathbf{A}\Delta\sigma_{\mathbf{v}_{j_k}} = \mathbf{b} + \mathbf{J}^T\lambda$
    $\mathbf{J}^T\Delta\sigma_{\mathbf{v}_{j_k}} = \delta$
    $\hat{\sigma}_{\mathbf{v}_{j_k}} = \sigma_{\mathbf{v}_{j\ k-1}} + \Delta\sigma_{\mathbf{v}_{j_k}} + Q_{\mathbf{v}}$
    $\hat{\sigma}_{\mathbf{x}_{j_k}} = \sigma_{\mathbf{x}_{j\ k-1}} + T\hat{\sigma}_{\mathbf{v}_{j_k}}$
  end
  $\hat{X}_k = \mathrm{E}[\hat{\sigma}_k^*]$
  $\hat{P}_k = \mathrm{cov}[\hat{\sigma}_k^*] + Q$;
  Correction:
  for $j = 1 : r$ **do**
    $\underline{\hat{Z}}_{j_k} = \mathbf{C}_+\,\underline{\hat{\sigma}}_{j_k}$ *see eq.* (18)
  end
  $P_k^{\hat{X}\hat{Z}} = \mathrm{cov}[\hat{\sigma}_k^*, \hat{Z}_k^*]$
  $P_k^{\hat{Z}} = \mathrm{cov}[\hat{Z}_k^*, \hat{Z}_k^*] + R$
  $K_k = P_k^{\hat{X}\hat{Z}}(P_k^{\hat{Z}})^{-1}$
  $X_k = \hat{X}_k + K_k(Z_k - \mathrm{E}[\hat{Z}_k^*])$
  $P_k = \hat{P}_k - P_k^{\hat{X}\hat{Z}}(P_k^{\hat{Z}})^{-1}(P_k^{\hat{X}\hat{Z}})^t$
end

Algorithm 1: UKF for physics-based constrained simulation. Index *i* is omitted in the notation.

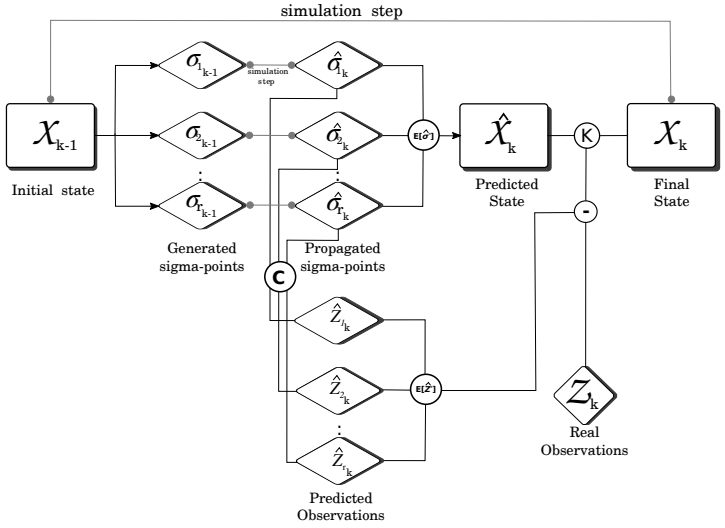

Figure 4: **Computation Overview**. One single simulation-step is composed of several filter-steps. Filter final state will provide the mechanical state of the catheter to be used in the following simulation step.

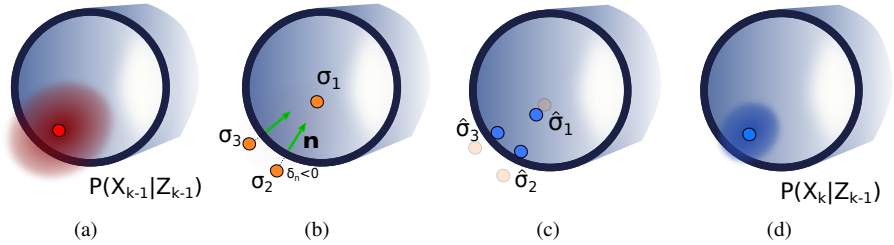

Figure 5: **Constrained State Estimation**.(a) Red dot represents a catheter node, described through a state vector and covariance. Green arrows define the inside of the surface. (b) Generated sigma-points may fall outside the geometry, behaving as interpenetrated objects $\boldsymbol{\delta_n} \leq 0$ (c) Their position is then corrected during propagation through collision response. (d) Predicted mean and covariance are hence computed from propagated samples.

From the simulation point of view, such scenario corresponds to a configuration of the catheter not respecting the constraint ($\boldsymbol{\delta_n} < 0$ in Fig. 5(b)). The collision response model presented in Sec. 2.2.2 enables to solve this problem. During the propagation step, nodes detected as crossing the vessel wall are corrected through contact forces, and projected back into the space of physically acceptable states (i.e. with positions inside the vessel) (see Fig.5). Furthermore, non-linear interactions with the surrounding surface, taking into account non-sliding contacts (see Eq. (6)), enables to further improve the prediction of the catheter shape. The proposed Bayesian filter process enables the fusion of mechanical constraints with the geometric constraints provided by 2D image features. The number of possible solutions to the ill-posed 2D-3D reconstruction problem is thereby reduced down to a single high probability, and correct, hypothesis in the vast majority of cases. Analyzing the covariance of the position of the catheter's node, allows to back up this assertion. In fact, the covariance of the position (i.e. its uncertainty) is greatly reduced when a contact occurs (see Fig. 6).

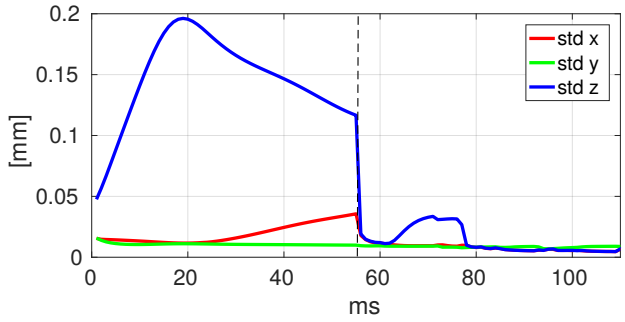

Figure 6: **Standard Deviation of Tip Position**. These results refer to the synthetic scenario performed in sec. 3.2. The contact occurring around $T \sim 55$ considerably reduces the standard deviation of the tip position. In addition, it is possible to notice how the uncertainty on Z-axis, i.e. the depth direction of the projective view, is greater than the uncertainty on X-axis and Y-axis, before any contact has occurred

3. Experimental Set-Up and Results

3.1. Overview and error metrics

We tested the method to retrieve the 3D shape of a navigating device from 2D images, both in a synthetic environment and in the real world. In both cases, a ground truth 3D shape was

available to compare our results with. Tests have been carried out to estimate the performance of the filter in the presence of different sources of model uncertainty, observation noise and parameters tuning. In particular, our validation aimed at demonstrating how our approach can naturally handle uncertainties related to model parameterization as well as observations obtained from different angles of view.

The quality of the reconstruction has been evaluated comparing 3D shape of the reconstructed catheter with a known ground-truth. Comparison metrics have been evaluated on B-spline interpolations, computed starting from the tip, of both the reference shape $\mathbf{g}_M = (g_1, ..., g_M)$ and the catheter's $\mathbf{c}_M = (c_1, ..., c_M)$, (with $M = 10N$ against the N nodes of the FE model). This allows to have a finer discretization of the shapes. We evaluated, the Euclidean distance between the reference tip and the reconstructed tip: $\mathbf{d}(\mathbf{g_M}, \mathbf{c_M}) = \sqrt{(g_1 - c_1)^2}$; the mean distance between the distal segment of the reference shape and the distal segment of the reconstructed shape: $\mathbf{m}(\mathbf{g_M}, \mathbf{c_M}) = \frac{1}{L}(\sqrt{\sum_{i=1}^{L}(g_i - c_i)^2}$, with $i \in [1, L]$ covering the 1cm distal part of the device, and the 3D Hausdorff distance between the whole ground truth shape and the reconstructed shape $\mathbf{h}(\mathbf{g_M}, \mathbf{c_M}) = \max_{g \in \mathbf{g}_M} (\min_{c \in \mathbf{c}_M}(\mathbf{d}(g, c)))$. We focused on the tip and distal segment of the device, because it is the part most subject to variations during the insertion and of the highest importance for clinicians.

3.2. *Synthetic Validation Set-Up*

The synthetic set-up provided a fully controlled ground truth and allowed to evaluate the robustness of the method to inaccuracies in the process model and to filter parameters tuning.

3.2.1. *Ground Truth Reference*

We simulated catheter insertion on two different geometries First, a Y-shaped surface, mimicking a vessel bifurcation, was generated by connecting 3 cylinders of 1 cm in diameter. A second geometry, extracted from an anatomical vascular phantom (see Sec. 3.3.3), has been used to simulate a more real scenario. In both cases, we generated a sequence of ground truth 3D shapes, using the deterministic model of physics-based simulation (presented in Sec. 2.2) with known model parameters. Overall, we have three different reference scenarios: two performed with the Y-shaped geometry and one with the anatomical vessel. Model parameterizations used to generate the 3 different ground truth scenarios are respectively summarized in tables 2, 3 and 4. The ground truth navigation was simulated mimicking a full insertion of the catheter along the total length of the vessel (10 cm).

3.2.2. *2D Observations*

2D image-features were generated by projecting the ground truth positions under two different view incidences (816 x 600 pixels, with a pixel size of 0.24 mm), (see Fig. 7 for the set-up in the Y-shaped geometry): one from the side where the view of the bifurcation is ambiguous (a catheter viewed in the vessels could be in any bifurcating branch), and one from the top with a clear view of the bifurcation.

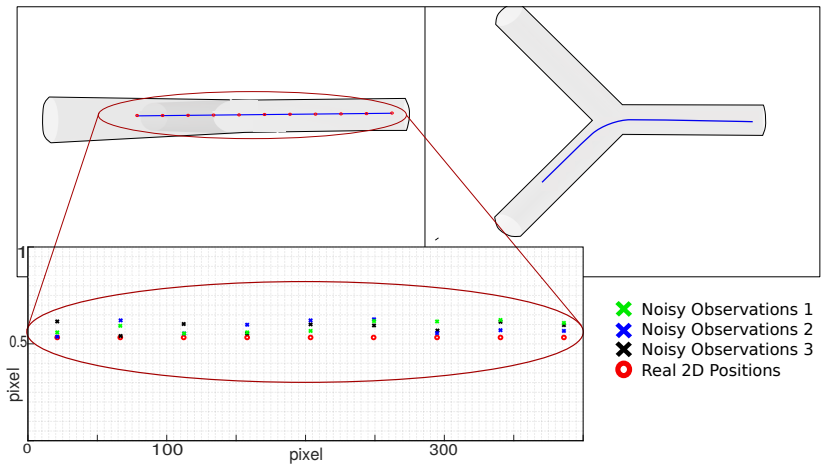

Figure 7: **Observations**. Two different views for 2D observations, side and top views. 2D observations were created by rendering the virtual catheter, equipped with markers, in each view, detecting the markers, and adding a Gaussian noise to their locations. Three instances of noisy observations were created for each view, adding a Gaussian noise of 0.1 pixel to Real 2D Positions.

At each time step of the simulated insertion, virtual markers placed on the catheter are projected through a known projection matrix and their 2D positions are automatically computed. 3 different observations sets were generated by adding a random Gaussian 2D noise to such projected 2D position. A standard deviation of 0.1 pixels was chosen to be consistent with the level of detection error encountered in actual images. Thereby, 6 different data-sets of 2D observations were generated.

3.2.3. Stochastic Environment: Filter Parameters Tuning

Filters parameters consist in: the initial state covariance $\boldsymbol{P}_0$, the process noise covariance $\boldsymbol{Q}$ and the observation noise covariance $\boldsymbol{R}$. Such parameters should be initialized to fit the actual level of noise tainting both the process and the observations, which is usually very difficult to set in practice. In our synthetic, fully controlled, environment, though, these parameters are either known ($\boldsymbol{R}$) or can be evaluated ($\boldsymbol{P}_0$ and $\boldsymbol{Q}$).

The covariance matrices $\boldsymbol{P}_0$ and $\boldsymbol{Q}$ have been estimated following a Monte Carlo approach based on multiple process configurations, characterized each by a certain model inaccuracy (see Fig. 8). In practice, we forecast multiple simulations characterized by a given model parameterization, which is incorrect with respect to the known ground truth (red shape in Fig. 8. Differences in model parameterization generate different catheter configurations (blue shapes in Fig. 8). Computing the average standard deviation of all the configurations positions and velocities, we initialize the uncertainty associated to the model (ν_k in Eq. (13)). The statistics on the positions and velocities were only computed on the distal segment of the catheter. This led us to set the computed values to initialize $\boldsymbol{P}_0$ (with covariances on both positions and velocities) and $\boldsymbol{Q}$ (with covariances only on velocities, see Eq. (13)), in a nominal configuration that we will call $\mathcal{P}_0$. To evaluate filter performance against its parameterization, we ran it with $\mathcal{P}_0$ and two additional parameters configurations: an overestimation $\mathcal{P}_{sup} = 1.75^2\mathcal{P}$ an underestimation $\mathcal{P}_{inf} = 0.25^2\mathcal{P}$. Besides, two observation noise covariance values were also considered: $\boldsymbol{R}_1$ and $\boldsymbol{R}_2$. As a consequence, the filter was run with 6 different parameterizations: $[\mathcal{P}, \boldsymbol{R}_1]$, $[\mathcal{P}, \boldsymbol{R}_2]$,

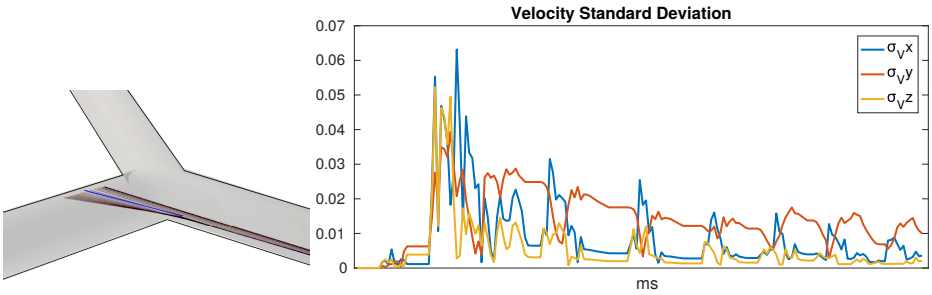

(a) Different model parameters generate different catheter's configurations

(b) Velocity Standard Deviation of Point at the Tip

Figure 8: **Filter Parameters Tuning** Initial values of $\boldsymbol{P}_0$ and $\boldsymbol{Q}$ are set through a Monte Carlo forecasting multiple simulations affected by different model parameterizations. (a) Different configurations due to errors in Young's Modulus. (b) Standard deviation of tip velocity, computed among different configurations obtained with different Young's Modulus.

$[\mathcal{P}_{sup},\ \boldsymbol{R}_1]$,$[\mathcal{P}_{sup}, \boldsymbol{R}_2]$, $[\mathcal{P}_{inf},\ \boldsymbol{R}_1]$, $[\mathcal{P}_{inf}, \boldsymbol{R}_2]$. Numerical values will be provided in following sections for each experiment.

3.2.4. Stochastic Environment: Process Model

Inaccuracies in the prediction by simulation are due do uncertainties on the FE model parameterization. The parameters which are known to influence the simulation are: intrinsic parameters such as the mass, stiffness and radius of the device, which appear in matrices $\mathbf{M}, \mathbf{B}, \mathbf{K}$ and extrinsic parameters such as contact forces or other applied forces which appear on the right hand side of Eq. (4).

In our context, we assume that mechanical parameters, such as mass, diameter, or Young modulus, can be determined either from literature or through simple measurements. In Fig. 9, we present a simple experiment showing the accuracy of our beam model. In practice, given a segment of catheter fixed at one extremity and undergoing simple gravity, we reproduce its behaviour through simulation and we evaluate whether the beam model provides a final configuration similar to the real layout. A Headway Duo device has been used and its mechanical parameters have been used for the FE model characterization (linear density 0.0359 [mg/cm], outer diameter 0.7 [mm], inner diameter 0.424 [mm]).

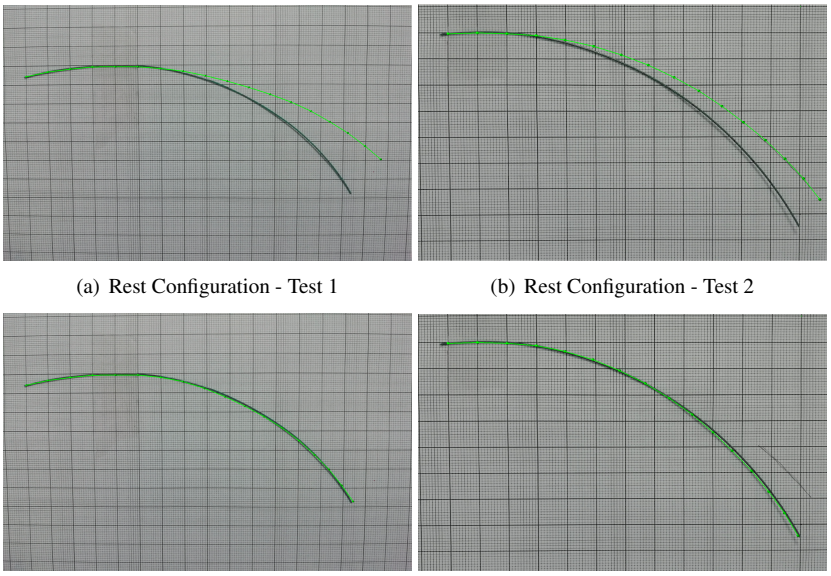

(a) Rest Configuration - Test 1 (b) Rest Configuration - Test 2

(c) Final Configuration - Test 1 (d) Final Configuration - Test 2

Figure 9: **Beam FE Model**. Starting from an initial configuration (green shape in (a) and (b) slightly curved due to the usage of the catheter) we reproduce with the simulation the behaviour of the device, fixed at one extremity and subject to gravity. Using the real mechanical parameter, we retrieve an accurate shape

A small uncertainty exists on the Young's modulus value, which was not given by the manufacturer. Using known values from literature, the simulation provided coherent results for an interval of 710 ± 110 [MPa]. Using the real mechanical parameter, we show the ability of the co-rotational FE model to retrieve an accurate configuration (mean 2D distance from real catheter 3.8 ± 2.1 [mm]). A parameter which could influence the behaviour of the simulation is the discretization of the beam (i.e. the number $N-1$ of serially linked elements). In Fig. 10, we show how differently discretized models, under the same mechanical parameters, lead to the same behaviour, except for the coarse model (d) which cannot retrieve the correct final configuration.

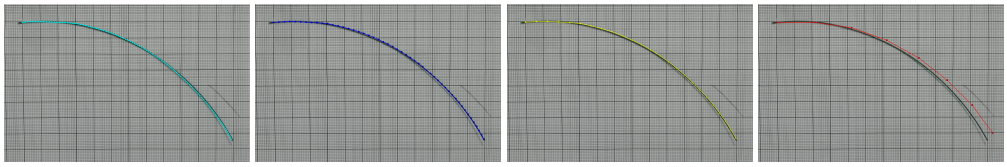

(a) N=100 (b) N=50 (c) N=25 (d) N=8

Figure 10: **Beam FE Model Discretization**. Coarser models deteriorate the mechanical behaviour. Results for $N = 10$ are shown in Fig. 10(c)-(d).

Other potential sources of uncertainty are represented by the forces applied to the device. Indeed, they are difficult to know with precision, and they are likely to vary along the path of the device. Contact forces hinge on the friction coefficient μ, which depends on several factors, such as patient anatomy, type of catheter, blood flow, etc. and cannot be known accurately. Whereas

the insertion force, which we assume to be constant during the navigation, can instead vary along the path due to the gesture of the clinician which is not constant. We show below, see Sec. 3.2, how these uncertain parameters may be added to the state vector, with the example of the force insertion.

*3.3. **Synthetic Environment Results***

We tested the sensitivity of the reconstruction to uncertainties on the friction coefficient, Young's modulus, initial configuration and applied forces. At the same time, we aimed at demonstrating how our approach can handle an ample range of model uncertainty, while providing valid results within a reasonable range of filter parameters tuning.

3.3.1. Sensitivity to Friction Coefficient for Y-Shaped Geometry

The friction coefficient μ is an impacting parameter in the case of simulation constrained due to collisions and it is hard to measure. In order to evaluate the impact of the misknowledge we will have in practice on such parameterization, As ground truth value, the friction coefficient was set according to literature [41] $\mu = 0.04$. we tested our filter with 20 different process model configurations, each corresponding to a different value for μ, ranging from 0 (i.e. no friction) to 0.08 (i.e. twice the ground truth value, and excluding the ground truth value 0.04) by steps of 0.004 (see Fig. 8). It is noteworthy that usual acceptable uncertainty lies in a range of 10-20%, but we wanted to test the filter capacity to deal with larger errors. Other parameters were the same as the reference model (Tab. 2).

	Ground Truth	**Incorrect Model**	unit
Young's Modulus	10	10	MPa
Radius	0.4	0.4	mm
Mass	0.5	0.5	g
Insertion Force	0.5e-03	0.5e-03	N/s
Total Length	9	9	cm
Time-step	0.001	0.001	s
Nodes	10	10	
Friction Coefficient	0.04	$\mathbf{0.04 \pm 0.04}$	

Table 2: Simulation parameters for friction coefficient sensitivity.

Filter parameter $\boldsymbol{P}_0$ has been initialized, according to Eq. (15) with $\sigma_{\mathbf{x}_{mod}} = [10^{-3}$ m, 10^{-5} deg] and $\sigma_{\mathbf{v}_{mod}} = [10^{-2}$ m/T, 10^{-3} deg/T]. Thus, $\boldsymbol{Q}$ was initialized with $\sigma_{mod} = \sigma_{\mathbf{v}_{mod}}$. Concerning the nominal observations noise covariance, we tested for two different instances: $\boldsymbol{R}_1 = (0.1)^2$ and $\boldsymbol{R}_2 = (0.01)^2$

The filter was able to provide an accurate estimate of the 3D catheter shape, even for important model uncertainties (i.e. $\mu = 0$, or $\mu = 0.08$). Errors were mainly noticeable in the depth direction and on the proximal part of the catheter, (Fig. 11 (a-c)), meaning that the distal segment was always accurately reconstructed (Fig. 11 (b-d)) due to the contact with the vessel surface. For a given observation data set and filter configuration, all the reconstructions presented the same error trend, indicating a behavior independent from model uncertainty. Nevertheless, the filter parameters $\mathcal{P}_{inf}$ provided the best results (see Fig. 11). The initial peak, common to all the graphs, is due to the filter starting-up. The effect of mechanical constraints on the quality of the reconstruction is particularly noticeable on Hausdorff distance that improves and stabilizes after the first contact (around $T = 250$). On average, for filter parameters $\mathcal{P}_{inf}$, we measured a

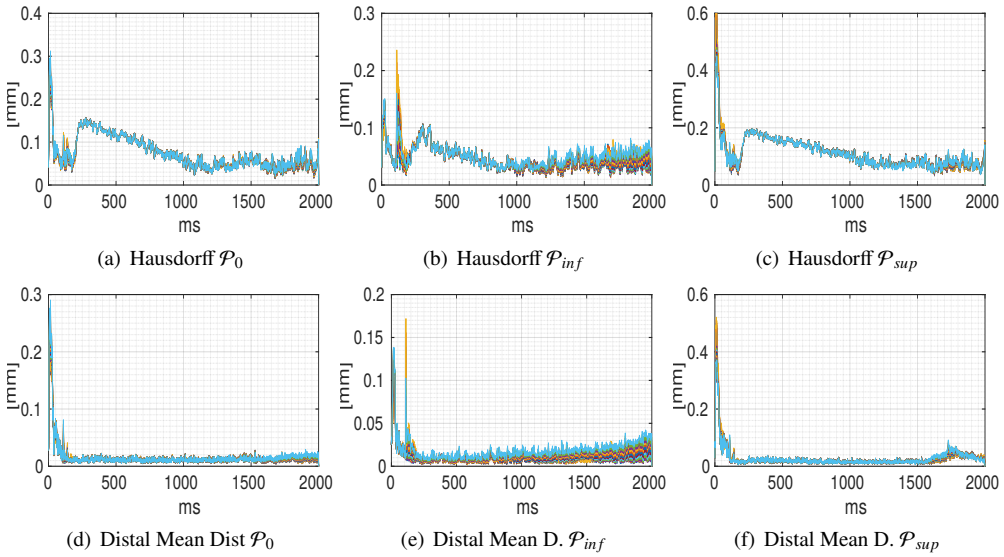

(a) Hausdorff $\mathcal{P}_0$ (b) Hausdorff $\mathcal{P}_{inf}$ (c) Hausdorff $\mathcal{P}_{sup}$

(d) Distal Mean Dist $\mathcal{P}_0$ (e) Distal Mean D. $\mathcal{P}_{inf}$ (f) Distal Mean D. $\mathcal{P}_{sup}$

Figure 11: **Sensitivity to Model Uncertainty**. Comparing metrics for different process model parameterization (21 curves on each plot). Observations from the side view were used and measurement noise covariance was $\mathbf{R}_1$. All reconstructions lay within the same range of accuracy showing the same trends, independent of the uncertainty on the model (error on μ).

3D Hausdorff distance of 0.07 ± 0.037 mm; a 3D distance at the tip equal to 0.021 ± 0.009 mm and a 3D mean distance on the distal segment of the catheter of 0.02 ± 0.008 mm. Such accurate results derive from the fact that this sensitivity analysis has been carried out assuming a globally limited uncertainty on the model: only the friction coefficient is misknown with respect to the real model.

3.3.2. Sensitivity to Generalized Model Uncertainties for Y-Shaped Geometry

In practice, models may present multiple uncertainties with respect to the real dynamics. In this section, we evaluate our filter performances when taking into account several incorrect parameters at the same time. A ground truth simulation of catheter navigation has been run on the Y-shaped geometry. Mass and diameters for catheter's models have been set according to manufacturer specifications for Headway Duo catheter (MicroVention Inc). Variations from ground truth have been taken into account for: Young's modulus, insertion force, friction coefficient and initial shape. Three different cases have been investigated. Models parameterizations are summarized in Tab. 3.

	Ground Truth	Case 1	Case 2	Case 3	unit
Young's Modulus	750	**250**	**500**	**1500**	MPa
Radius	0.35-0.02	0.35-0.02	0.35-0.02	0.35-0.02	mm
Mass	0.48	0.48	0.48	0.48	g
Insertion Force	1.7e-03	1.7e-03	**1.7e-04**	**1.7e-02**	N/s
Time-step	0.001	0.001	0.001	0.001	s
Total Length	10	10	10	10	cm
Nodes	31	**10**	**10**	**10**	
Friction Coefficient	0.01	**0.1**	**0**	**0.01**	
Initial Configuration	c_0	c_0	$c_0 \cdot [R\|T_c]$	$c_0 + T_c$	

Table 3: Simulation parameters for sensitivity test to multiple model uncertainties. See Fig. 13 for reference configuration c_0 (blue shape).

Analogously to previous section, observations have been acquired from side and top view as in Sec. 3.2.2. The nominal configuration $\mathcal{P}_0$ was set with: $\boldsymbol{P} \sim \sigma_{\mathbf{x}_{mod}} = [10^{-3}\,\text{m}, 0\,\text{deg}]$ and $\sigma_{\mathbf{v}_{mod}} = [10^{-3}\,\text{m/T}, 10^{-3}\,\text{deg/T}]$, and $\boldsymbol{Q} \sim \sigma_{mod} = [10^{-2}\,\text{m/T}, 10^{-2}\,\text{deg/T}]$. In this case, the model uncertainty $\boldsymbol{Q}$ is greater due to the several model uncertainties. Concerning the nominal observations noise covariance, we tested for three different instances: $\boldsymbol{R}_1 = (0.1)^2$, $\boldsymbol{R}_2 = (0.01)^2$ and $\boldsymbol{R}_2 = (0.001)^2$.

Case 1 (Tab.3): we considered uncertainties on Young's modulus and friction coefficient. Averaging results for all filter parameterization and both top and side observations, we obtained a 3D Hausdorff distance of 1.15 ± 0.15 mm; a 3D distance at the tip equal to 0.07 ± 0.05 mm and a 3D mean distance on the distal segment of the catheter of 0.13 ± 0.09 mm.

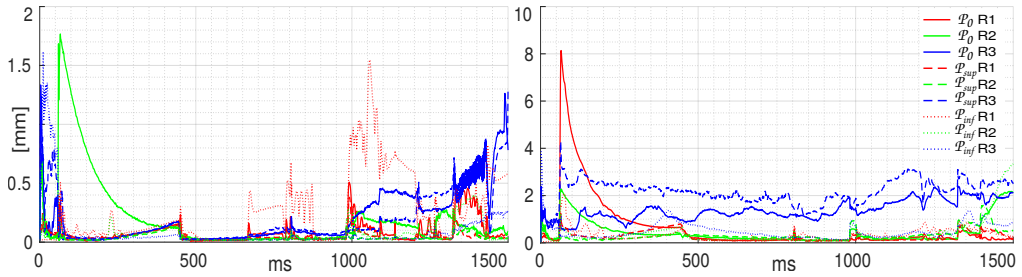

(a) Distal Mean Distance (b) Hausdorff Distance

Figure 12: **Case 1**. Average metrics evaluated between ground truth shape and reconstructed shape. All filter parameterization provide good results. Whenever $\boldsymbol{R}$ is small and $\boldsymbol{Q}$ is higher, a greater error appears at tail of the catheter, in the depth direction: (b) blue graphs.

All filter parameterizations allowed to retrieve an accurate 3D shape. Whenever a small $\boldsymbol{R}$ is combined with higher $\boldsymbol{Q}$, a larger error appears at the tail of the catheter (Fig. 12-(b) blue graphs); this is due to a greater trust in 2D observations (small $\boldsymbol{R}$) which intrinsically have an uncertainty in the depth direction.

Case 2 : besides erroneous model parameterization, we considered a different initial configuration (Fig. 13-(b), real blue shape against incorrect red shape). On average (for all filter parameterizations and views), the 3D Hausdorff distance was of 2.29 ± 1.27 mm, the 3D mean distance on the distal segment of 0.26 ± 0.25 mm and the 3D error at the tip of 0.13 ± 0.15 mm. The initial peak is due to the mismatch of the initial configuration, which is compensated by the filter after few time steps.

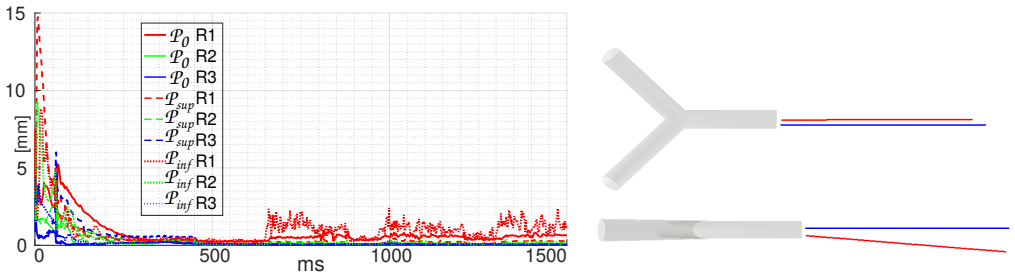

(a) Distal Mean Distance (b) Different Initial Configuration

Figure 13: **Case 2**. Distal mean distance between ground truth distal segment and reconstructed catheter distal segment. Blue shape c_0, red shape $c_0 \cdot [R|T_c]$

Case 3: we considered model's parameters errors plus a wrong initial configuration, symmetric with respect to the real one. In practice, the red model would naturally go towards the opposite branch. In case of 2D observations from a top view, the filter is able to compensate for model uncertainties and retrieve the correct shape. Instead, in case of perfectly horizontal observations, it is not possible to solve the ambiguity: the filter would not be able to reconstruct the catheter in the right direction and the reconstructed shape will diverge from the ground truth (Fig. 14). Nevertheless, a slight rotation of the camera with respect to the horizontal axis ($\sim 5°$ as shown in Fig.15-(b)) allows to solve the ambiguity and retrieve the correct 3D shapes, obtaining on average a 3D Hausdorff distance of 1.14 ± 1.25 mm; a 3D distance at the tip equal to 0.23 ± 0.15 mm and a 3D mean distance on the distal segment of the catheter of 0.40 ± 0.29 mm.

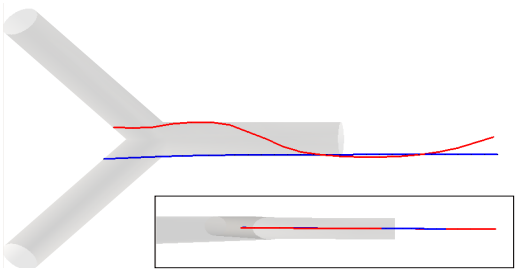

Figure 14: **Case 3**. A perfectly horizontal view, does not allow to solve the ambiguity, whenever the model would naturally go towards the wrong branch.

3.3.3. Sensitivity to Generalized Model Uncertainties for Vessel Geometry

Lastly, we performed similar synthetic evaluation, taking into account a more complex geometry extracted from real anatomy (Fig. 16-(a)). The vessel is 13cm long with an average diameter of 7mm. Mechanical characterization of catheter model has been set according to manufacturer specifics for Headway TM 17 catheter (MicroVention Inc.), which is the device used for the experiment on real data of Sec. 3.5). Parameters are summarized in Table 4.

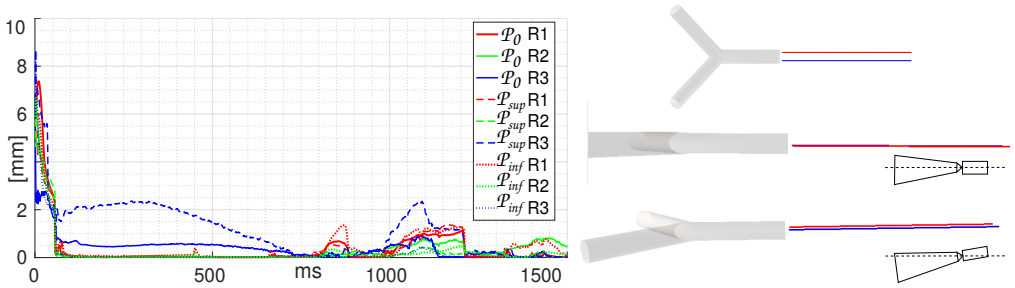

(a) Distal Mean Distance (b) Oblique View

Figure 15: **Case 3**.The ambiguity is easily solved by having a side view, slightly rotated with respect to the horizontal axis

	Ground Truth	**Incorrect Model**	unit
Young's Modulus	300	**400**	MPa
Radius	0.4-0.215	0.4-0.215	mm
Mass	0.1	0.1	g
Insertion Force	0.01	**0.0001**	N/s
Total Length	6	6	cm
Time-step	0.001	0.001	s
Nodes	21	**11**	
Friction Coefficient	0.1	**0.2**	

Table 4: Simulation parameters for sensitivity test on synthetic vessel geometry.

In this testbed, we simulate a clinical scenario where the real insertion force cannot been known (unless embedding the device with a sensor force). In order to take into account such uncertainty and improve the estimation, we add to the state vector such force and estimate its value.

$$\boldsymbol{X} = [\mathbf{x}_1^t, \mathbf{v}_1^t, ..., \mathbf{x}_N^t, \mathbf{v}_N^t, \mathbf{f}^t] \tag{20}$$

We assume the catheter to be inserted with a constant 6DoF force, applied to the bottom of the device. In practice, such force is not constant but varies through time with the gesture of the clinician. In order to take into account such error of modeling, we assume it to be constant through time except for a Gaussian error $\mathbf{f}_{T+1} = \mathbf{f}_T + \sigma_{\mathbf{f}_{mod}}$. Thus, the initial state covariance matrix $\boldsymbol{P}_0$ and the model covariance matrix $\boldsymbol{Q}$ are modified as follows:

$$\boldsymbol{Q} = \begin{pmatrix} \mathbf{I}_N \otimes \begin{pmatrix} \mathbf{0}_{6\times6} & \mathbf{0}_{6\times6} \\ \mathbf{0}_{6\times6} & \sigma^2_{\mathbf{mod}}\mathbf{I}_6 \end{pmatrix} & \mathbf{0}_{12N\times6} \\ \mathbf{0}_{6\times12N} & \mathbf{0}_{6\times6} \end{pmatrix} \tag{21}$$

$$\boldsymbol{P}_0 = \begin{pmatrix} \mathbf{I}_N \otimes \begin{pmatrix} \sigma^2_{\mathbf{x}_{mod}}\mathbf{I}_6 & \mathbf{0}_{6\times6} \\ \mathbf{0}_{6\times6} & \sigma^2_{\mathbf{v}_{mod}}\mathbf{I}_6 \end{pmatrix} & \mathbf{0}_{12N\times6} \\ \mathbf{0}_{6\times12N} & \sigma^2_{\mathbf{f}_{mod}}\mathbf{I}_{6\times6} \end{pmatrix} \tag{22}$$

As previously, different filter parameterizations have been taken into account. Observations have been acquired according view in Fig. (16-(a)) and noised with Gaussian additive. Although all filter parameters combinations provide similar results, best performances have been achieved with filter parameters combination $\mathcal{P}_0$, with an average 3D Hausdorff Distance of 0.81 ± 0.53

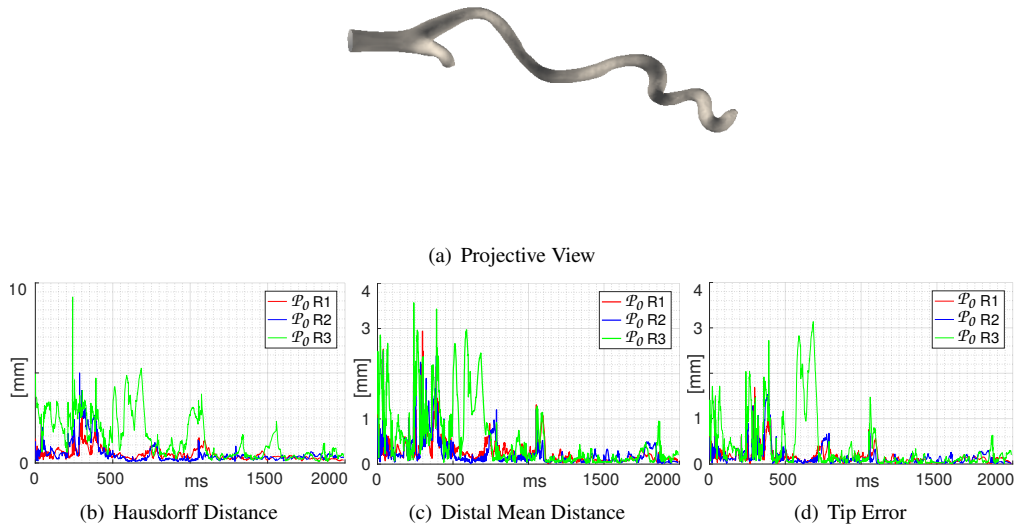

(a) Projective View

(b) Hausdorff Distance (c) Distal Mean Distance (d) Tip Error

Figure 16: **Evaluation Metrics for Synthetic Vessel Geometry**. Metrics provided for filter parameters combination $\mathcal{P}_0$. Whenever $\boldsymbol{R}$ is small (green graph), reconstruction appears less accurate due to the confidence given to observations which have an intrinsic uncertainty in depth direction.

mm, a 3D mean distance at the segment of 0.37 ± 0.17 mm and a 3D tip error of 0.24 ± 0.13 mm.

3.4. Experiments on Real Data

3.4.1. Ground Truth Reference

The real data-set was acquired using the testbed described in [42]. A 1.7F micro-catheter (Headway TM 17, MicroVention Inc.) was inserted in a rigid phantom made of a silicon mould of an internal carotid artery (H+N-R-A-003 model, Elastrat). This navigation within the transparent phantom was captured at 198 frames per second by a pair of two high speed cameras (TM-6740CL, JAI/Pulnix), synchronized using a trigger (C320 Machine Vision Trigger Timing Controller, Gardasoft). The stereovision camera setup was calibrated using a chessboard target and OpenCV algorithms. One camera was placed above the phantom, to provide a top view, and the other one provided the side view. In particular, the calibration measured the projection matrices for each view (matrix $\mathbf{C}$ in Eq. ((18))).

A sequence of 2130 images (640 x 480 pixels, with a pixel size of 0.13 mm), of a total duration of 10 s, was acquired: the catheter was automatically segmented and reconstructed in 3D by triangulation in each frame. This provided the ground truth reconstruction. The reconstruction error was estimated to be below 0.05 mm on 1000 images of a motionless catheter. In this sequence, a stick and slip transition occurred around frame number $T = 1300$ (see Fig. 19, (f)-(h)). The speed of the catheter tip was estimated to peak at 500 mm/s in the slip phase.

3.4.2. FE model parameterization and 2D Observations

The catheter length was 6 cm at the end of the insertion. Thereafter, the catheter was modeled as a series of 11 connected beams, of 5.5 mm each (12 nodes). Without further knowledge on the physical properties of the material used (silicon, catheter, slippery liquid infused in the phantom...) the friction coefficient was set to $\mu = 0.1$, other mechanical properties such as mass, diameter and Young's modulus have been set according to manufacterers specifics (see Tab.4, ground truth). Concerning the insertion force, it has been set set according to the velocity values provided for the catheter motion in [42] ($\mathbf{f}_1$=0.8e-03 N/timeStep). A second force intensity has been tested ($\mathbf{f}_2$=2.5e-03 N/timeStep), to simulate uncertainties occurring in reality.

The detection of markers is out of the scope of this paper. Furthermore, the catheter did not carry any visible marker in the images. The 2D observations were therefore generated in a similar way as in the synthetic setup: virtual markers were placed along the ground truth shapes and reprojected in each frame, a Gaussian noise (with standard deviation of 0.1 pixel) was added to their locations.

3.4.3. Stochastic Environment: Filter Parameter Tuning

In this experiment, in order to accelerate the computation time, we used the reduced state vector with 9 components per node (no orientation, see Sec. 2.4.4). As the synthetic vessel scenario, we considered the insertion force within the state vector, still described with the model $\mathbf{f}_{T+1} = \mathbf{f}_T + \sigma_{\mathbf{f}_{mod}}$. Filter parameters have been initialized as the previous experiment. In particular, for $\mathbf{f}_1$=0.8e-03 N/timeStep the covariance was initialized with $\sigma_{\mathbf{f}_{1mod}} = 0.4e-03$, while for $\mathbf{f}_2$=2.5e-03 N/timeStep we set $\sigma_{\mathbf{f}_{2mod}} = 1e-03$.

3.5. *Real Data Results*

3.5.1. Filter parameterization

Fig. 17 and 18 reports the evaluation metrics between the retrieved shape and the ground truth, when initializing the model with two different insertion forces. We present the results for the filter parameters combination $\mathcal{P}_{sup}$, but all the three parameters configuration provided similar results. Only the average 3D distance on the distal segments is displayed, but all the metrics presented similar behaviors. All the configurations present a peak around $T \sim 1300$. This is due to the filter response to the stick and slip transition, a phenomenon where the cumulative effect of the friction force causes an abrupt movement of the device. The filter was able to rapidly recover from such a sudden variation in positions and velocities.

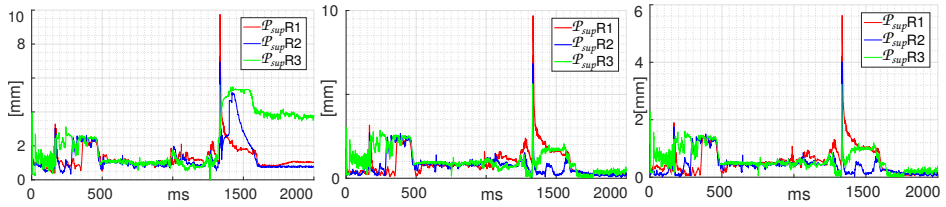

(a) Hausdorff Distance (b) Distal Mean Distance (c) Tip Error

Figure 17: **Evaluation Metrics for $\mathbf{f}_1$=0.8e-03 N/timeStep**.

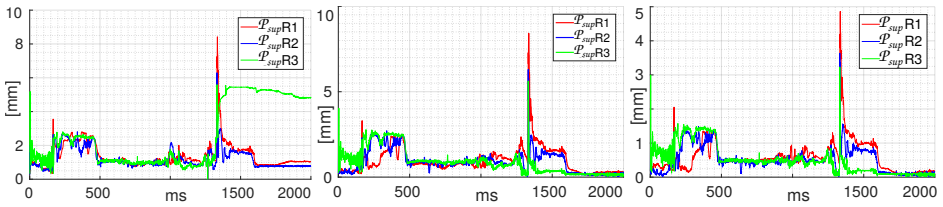

(a) Hausdorff Distance (b) Distal Mean Distance (c) Tip Error

Figure 18: **Evaluation Metrics for f_2=2.5e-03 N/timeStep**.

Taking into account the forces within the state vector, allows high uncertainty on how the insertion forces are modeled. On average, we obtained a 3D Hausdorff distance of 1.74 ± 0.77 mm, a 3D mean distance at the distal segment of 0.91 ± 0.14 mm, a 3D error on the tip of 0.53 ± 0.09 mm. In Fig. 19, we present qualitative reconstruction results: the side view was used for the observation data (observation view), and the reconstructed catheter is here superimposed (in green) over validation view (orthogonal to the observation view), to demonstrate how the physics-based constrained simulation helps to accurately recover the depth of the catheter.

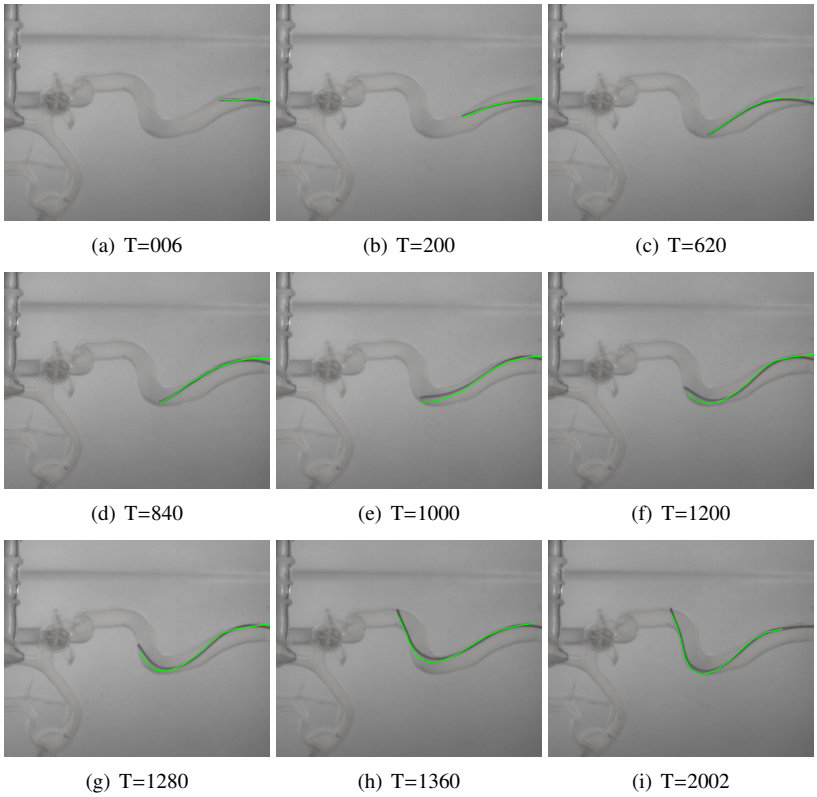

(a) T=006 (b) T=200 (c) T=620

(d) T=840 (e) T=1000 (f) T=1200

(g) T=1280 (h) T=1360 (i) T=2002

Figure 19: **Qualitative Validation** The reconstructed shapes are superimposed in the validation view (view orthogonal to the observation view). In fig. (f), (g), (h) it is possible to observe the stick and slip transition where an abrupt movement happens within a short interval (for more details see [42].

3.5.2. Reducing the number of markers

Our method relies on the presence of opaque markers placed along the catheter. This is not the case for most current catheters. Whereas the state vector keeps its configuration as in Eq. (20), with $N = 12$; we test filter performances for different number of markers (respectively $3, 6, 12$), equally distributed along the catheter shape (see Fig. 20).

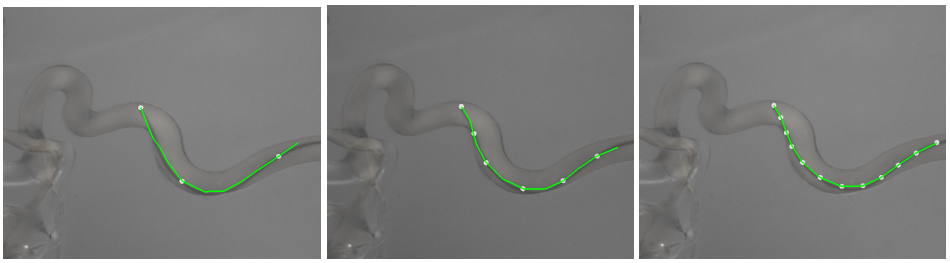

(a) 3 Observed Markers (b) 6 Observed Markers (c) 12 Observed Markers

Figure 20: **Number of Observed Markers** Validation view (view orthogonal to the observation view) for $T \sim 1300$

Decreasing the number of observed markers, with respect to the number of nodes in the state vector, globally degrades the quality of the reconstruction. This is particularly clear in Fig. 20, where the filter precision is reduced when using 3 observed markers, the filter is no more able to handle the stick and slip transition occurring at $T \sim 1300$. Reconstruction performed with 12 or 6 observed markers allows to gather similar results (blue and red graph in Fig. 21).

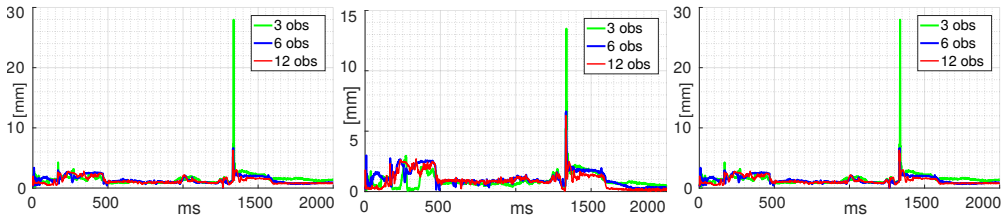

(a) Hausdorff Distance (b) Distal Mean Distance (c) Tip Error

Figure 21: **Evaluation Metrics for Different Numbers of Observed Markers** Although 12 observed markers (1 marker per model node) provide the best results, red graph, simular performances are obtained using 6 observations (blue graph). Reducing the observed markers to 3, entails a degradation in filter accuracy, especially around $T \sim 1200$ where stick and slip transition occurs. Having only 3 observations the filter is not able to retrieve immediately the correct configuration, and the error between the ground truth shape and the reference one increase (green graph).

In another experience, we kept the one to one mapping between the markers and nodes, iteratively reducing both of them. Indeed, reducing the number of nodes, proportionally impacts the state vector and thereafter the filter processing time performances. When the number of observations was divided by two (6 markers/nodes, see Fig. 22), the filter could reconstruct the catheter when its motion was smooth and gradual. However, a loss of accuracy was observed after the stick and slip transition. Indeed, fewer observations, especially along the distal segment, entails a loss of information on the curvature of the device, which is extremely flexible and may undergo important deformations, like during the stick and slip transitions.

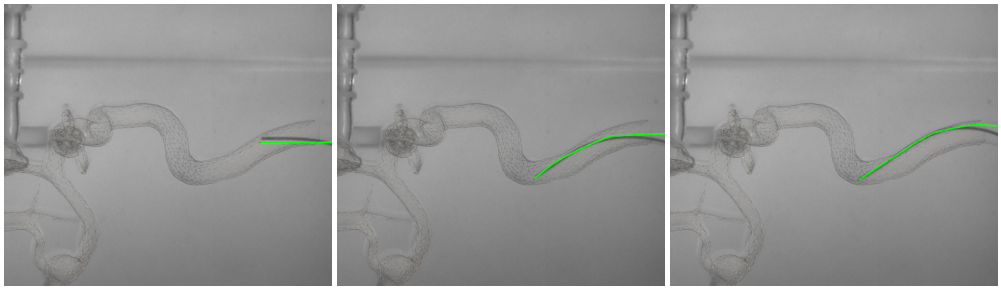

(a) T~110 (b) T~400 (c) T~800

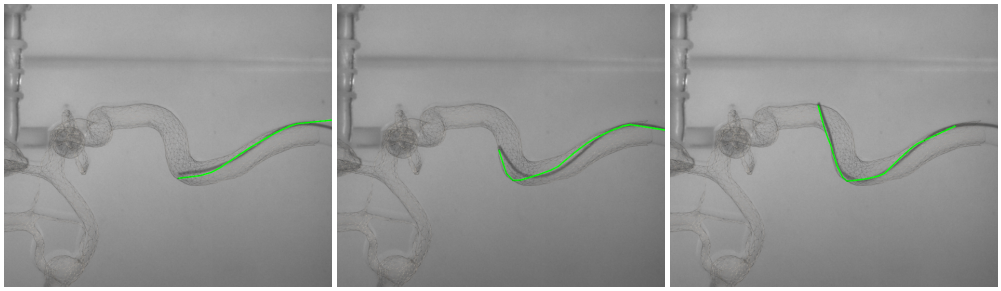

(d) T~1000 (e) T~1200 (f) T~1700

Figure 22: **Validation view using 6 observations and 6 nodes**. Reconstruction appears less smooth compared to the background real image.

This was confirmed when further reducing the number of markers/nodes down to 3 (Fig. 23). The sparsity of the observations implies a lack of information about the bending of the device, which does not allow the filter to retrieve the correct 3D shape of the device.

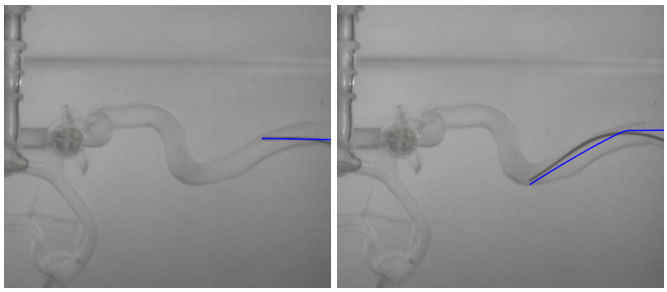

(a) T~110 (b) T~400

Figure 23: **Validation view using 3 observations and 3 nodes**. Such configuration does not allow to retrieve the correct curvature of the device.

4. Discussion and Conclusion

In a very common routine practice, radiologists navigate catheters through the vascular network under the visual guidance of single plane fluoroscopy images. This implies for the radiologist to infer the 3D shape of the device from a monocular view, which has been long known

to be an ill-posed problem. Although recent progress in physics-based simulation have enabled realistic interactive virtual navigation, the 3D computed shape remains sensitive to even small uncertainties in the value of mechanical parameters, such as the friction coefficient.

To go beyond these limitations, we have proposed to embed a physics-based simulation in a Bayesian filtering framework where 2D observations are based on radio-opaque markers placed on the catheter detected in the fluoroscopic images. An Unscented Kalman Filter formulation was provided and was experimented in both synthetic setup and real phantom data. Both quantitative and qualitative results demonstrate the ability of our method to recover an accurate 3D shape at interactive time frames, under a variety of filter parameterizations and challenging conditions: inaccurate friction coefficient and ambiguous views (synthetic scenario), non-linear complex contacts and abrupt stick and slip motions (real data set). The optimal filter parameterization could easily be deduced from practical considerations on the model uncertainty, but the standard deviation on the observation noise had to be underestimated by an order of magnitude. This question is part of our current investigations, but we believe that an offline calibration step could provide adequate values, to be used during the clinical procedure.

As presented in our results, including parameters in the state vector, in particular the insertion force, allows to globally improve the estimation. We recently started to investigate the optimal markers/node configuration to reach the best compromise between practical setup, accuracy of the reconstruction, and simulation time. In conclusion, the number of observed markers and nodes depends on the rigidity of the device and the deformations it will be subject to. More rigid devices, like needles, could be reconstructed from a very small number of observations. But in the case of a catheter, a good design would probably adapt the number of markers to both the flexibility and the accuracy required by the application, and would therefore position more markers on the distal segment, and only a few markers on the proximal portion. Such configuration must be compatible with the device's design requirements. More in general, future works aim at improving the validation of our method to bring it closer to clinical application. For example, fluoroscopic images are usually captured at 30 frames per second, which is 6 times slower than our high speed cameras. As a consequence, catheter motions in-between two consecutive frames might be larger. Even though our experiments proved that our algorithm could handle large motions, we believe a device should be used in practice to capture the motion induced by the practitioner on the device. This motion would serve as input to the simulation for a better model prediction. As another example, in order to retrieve the 3D shape of non-tagged devices, such as guidewires, we need to implement a marker-less method. Such assumption would require to define a different observation function which relates the state vector with the observed 2D features. In case of tagged-device, the observation function is basically a constant mapping between the detected 2D markers and the 3D nodes of the FE model, related the one to the others through a projection matrix. In case of non-tagged device, defining an observation function would not be so straightforward, given that no 2D positions would be directly detected in fluoroscopic images. In this case, 2D-3D correspondence between 2D segments (curves) and 3D point cannot be done through a constant mapping and a more robust observation function must be defined. This last, and other optimization aspects, will be investigated in future works.

References

[1] P. R. DeLucia, R. D. Mather, J. A. Griswold, S. Mitra, Toward the Improvement of Image-Guided Interventions for Minimally Invasive Surgery: Three Factors That Affect Performance, Human Factors: The Journal of the Human Factors and Ergonomics Society 48 (1) (2006) 23–38 (2006).

[2] S. Gorges, E. Kerrien, M. Berger, Y. Trousset, J. Pescatore, R. Anxionnat, L. Picard, S. Bracard, 3D augmented fluoroscopy in interventional neuroradiology: Precision assessment and first evaluation on clinical cases, Workshop on Augmented environments for Medical Imaging and Computer-aided Surgery-AMI-ARCS 2006 (2006) 11–06 (2006).

[3] W. Ahmad, H. C. Hasselmann, N. Galas, P. Majd, S. Brunkwall, J. S. Brunkwall, Image fusion using the two-dimensional-three-dimensional registration method helps reduce contrast medium volume, fluoroscopy time, and procedure time in hybrid thoracic endovascular aortic repairs, J. Vasc. Surg. 69 (4) (2019) 1–8 (apr 2019).

[4] S. Albarqouni, U. Konrad, L. Wang, N. Navab, S. Demirci, Single-view x-ray depth recovery: toward a novel concept for image-guided interventions, International journal of computer assisted radiology and surgery 11 (6) (2016) 873–880 (2016).

[5] C. Baur, S. Albarqouni, S. Demirci, N. Navab, P. Fallavollita, Cathnets: detection and single-view depth prediction of catheter electrodes, in: International Conference on Medical Imaging and Augmented Reality, Springer, 2016, pp. 38–49 (2016).

[6] S. Baert, E. van de Kraats, T. van Walsum, M. Viergever, W. Niessen, Three-dimensional guide-wire reconstruction from biplane image sequences for integrated display in 3-d vasculature, IEEE Transactions on Medical Imaging 22 (10) (2003) 1252–1258 (oct 2003).

[7] M. Hoffmann, A. Brost, C. Jakob, F. Bourier, M. Koch, K. Kurzidim, J. Hornegger, N. Strobel, Semi-automatic catheter reconstruction from two views, in: International Conference on Medical Image Computing and Computer-Assisted Intervention, Springer, 2012, pp. 584–591 (2012).

[8] C. Delmas, M.-O. Berger, E. Kerrien, C. Riddell, Y. Trousset, R. Anxionnat, S. Bracard, Three-dimensional curvilinear device reconstruction from two fluoroscopic views, in: SPIE, Medical Imaging 2015: Image-Guided Procedures, Robotic Interventions, and Modeling, Vol. 9415, San Diego, CA, United States, 2015, p. 94150F (Feb. 2015).

[9] S. Condino, V. Ferrari, C. Freschi, A. Alberti, R. Berchiolli, F. Mosca, M. Ferrari, Electromagnetic navigation platform for endovascular surgery: how to develop sensorized catheters and guidewires., The international journal of medical robotics and computer assisted surgery : MRCAS 8 (3) (2012) 300–10 (sep 2012).

[10] S. Pujol, M. Pecher, J.-L. Magne, P. Cinquin, A virtual reality based navigation system for endovascular surgery., Studies in health technology and informatics 98 (2004) 310–2 (jan 2004).

[11] A. Schwein, B. Kramer, P. Chinna Durai, S. Walker, M. O'Malley, A. Lumsden, J. Bismuth, Flexible Robotics With Electromagnetic Tracking Improve Safety and Efficiency During In Vitro Endovascular Navigation, Journal of Vascular Surgery 63 (1) (2016) 285–286 (jan 2016).

[12] P. T. Tran, P.-L. Chang, H. De Praetere, J. Maes, D. Reynaerts, J. V. Sloten, D. Stoyanov, E. V. Poorten, 3D Catheter Shape Reconstruction Using Electromagnetic and Image Sensors, Journal of Medical Robotics Research 02 (03) (2017) 1740009 (2017).

[13] A. M. Franz, T. Haidegger, W. Birkfellner, K. Cleary, T. M. Peters, L. Maier-Hein, Electromagnetic tracking in medicine—a review of technology, validation, and applications, IEEE transactions on medical imaging 33 (8) (2014) 1702–1725 (2014).

[14] T. van Walsum, S. Baert, W. Niessen, Guide wire reconstruction and visualization in 3DRA using monoplane fluoroscopic imaging, IEEE Transactions on Medical Imaging 24 (5) (2005) 612–623 (may 2005).

[15] T. Petković, R. Homan, S. Lončarić, Real-time 3D position reconstruction of guidewire for monoplane X-ray, Computerized Medical Imaging and Graphics 38 (3) (2014) 211–223 (2014).

[16] M. Brückner, F. Deinzer, J. Denzler, Temporal estimation of the 3d guide-wire position using 2d X-ray images, Lecture Notes in Computer Science (including subseries Lecture Notes in Artificial Intelligence and Lecture Notes in Bioinformatics) 5761 LNCS (PART 1) (2009) 386–393 (2009).

[17] M. Groher, F. Bender, A. Khamene, W. Wein, T. H. Heibel, N. Navab, 3d guide wire navigation from single plane fluoroscopic images in abdominal catheterizations, in: Bildverarbeitung für die Medizin 2009, Springer, 2009, pp. 356–360 (2009).

[18] R. Trivisonne, E. Kerrien, S. Cotin, Augmented 3D Catheter Navigation using Constrained Shape from Template (2017).

[19] A. Dore, G. Smoljkic, E. V. Poorten, M. Sette, J. V. Sloten, G. Z. Yang, Catheter navigation based on probabilistic fusion of electromagnetic tracking and physically-based simulation, in: IEEE International Conference on Intelligent Robots and Systems, 2012, pp. 3806–3811 (2012).

[20] A. Malti, R. Hartley, A. Bartoli, J. H. Kim, Monocular template-based 3d reconstruction of extensible surfaces with local linear elasticity, Proceedings of the IEEE Computer Society Conference on Computer Vision and Pattern Recognition (2013) 1522–1529 (2013).

[21] N. Haouchine, J. Dequidt, M. O. Berger, S. Cotin, Monocular 3D Reconstruction and Augmentation of Elastic Surfaces with Self-Occlusion Handling, IEEE Transactions on Visualization and Computer Graphics 21 (12) (2015) 1363–1376 (2015).

[22] A. Malti, C. Herzet, Elastic shape-from-template with spatially sparse deforming forces, Proceedings - 30th IEEE

Conference on Computer Vision and Pattern Recognition, CVPR 2017 2017-January (2017) 143–151 (2017).
[23] A. Agudo, F. Moreno-Noguer, Force-Based Representation for Non-Rigid Shape and Elastic Model Estimation, IEEE Transactions on Pattern Analysis and Machine Intelligence 40 (9) (2018) 2137–2150 (2018).
[24] A. Agudo, F. Moreno-Noguer, B. Calvo, J. M. Montiel, Real-time 3D reconstruction of non-rigid shapes with a single moving camera, Computer Vision and Image Understanding 153 (2016) 37–54 (2016).
[25] A. Agudo, F. Moreno-Noguer, B. Calvo, J. M. Montiel, Sequential Non-Rigid Structure from Motion Using Physical Priors, IEEE Transactions on Pattern Analysis and Machine Intelligence 38 (5) (2016) 979–994 (2016).
[26] S. J. Julier, J. K. Uhlmann, New extension of the Kalman filter to nonlinear systems, in: Int. Symp. Aerospace/Defense Sensing, Simul. and Controls, 1997, pp. 182–193 (1997).
[27] R. E. Kalman, Others, A new approach to linear filtering and prediction problems, Journal of basic Engineering 82 (1) (1960) 35–45 (1960).
[28] R. Brown, P. Hwang, Introduction to Random Signals and Applied Kalman Filtering with MatLab Excercises Fourth Edition, Wiley, 2011 (2011).
[29] P. Moireau, D. Chapelle, Reduced-order Unscented Kalman Filtering with application to parameter identification in large-dimensional systems, ESAIM: Control, Optimisation and Calculus of Variations 17 (2) (2011) 380–405 (2011).
[30] H. Wang, J. Wu, M. Wei, X. Ma, A robust and fast approach to simulating the behavior of guidewire in vascular interventional radiology, Computerized Medical Imaging and Graphics 40 (2015) 160–169 (2015).
[31] S. Timoshenko, On the correction for shear of the differential equation for transverse vibrations of prismatic bars, The London, Edinburgh, and Dublin Philosophical Magazine and Journal of Science 41 (245) (1921) 744–746 (may 1921).
[32] C. A. Felippa, B. Haugen, A unified formulation of small-strain corotational finite elements: I. theory, Computer Methods in Applied Mechanics and Engineering 194 (21-24) (2005) 2285–2335 (2005).
[33] S. Cotin, C. Duriez, J. Lenoir, P. Neumann, S. Dawson, New approaches to catheter navigation for interventional radiology simulation., MICCAI 8 (2005) 534–542 (jan 2005).
[34] D. Baraff, A. Witkin, Large steps in cloth simulation, Proceedings of the 25th annual conference on Computer graphics and interactive techniques - (SIGGRAPH '98) (1998) 43–54 (1998).
[35] C. Duriez, F. Dubois, A. Kheddar, C. Andriot, Realistic Haptic Rendering of Interactive Deformable Objects in Virtual Environments, IEEE Transactions on Visualization and Computer Graphics 12 (1) (2006) 36–47 (2006).
[36] H. Courtecuisse, J. Allard, P. Kerfriden, S. P. Bordas, S. Cotin, C. Duriez, Real-time simulation of contact and cutting of heterogeneous soft-tissues, Medical Image Analysis 18 (2) (2014) 394–410 (2014).
[37] P. Ambrosini, D. Ruijters, W. J. Niessen, A. Moelker, T. V. Walsum, Fully Automatic and Real-Time Catheter Segmentation in X-Ray Fluoroscopy, in: MICCAI 2017, Vol. 8150, 2017, pp. 577–585 (2017).
[38] N. Honnorat, R. Vaillant, N. Paragios, Graph-based geometric-iconic guide-wire tracking, in: G. Fichtinger, A. Martel, T. Peters (Eds.), Medical Image Computing and Computer-Assisted Intervention – MICCAI 2011, Springer Berlin Heidelberg, Berlin, Heidelberg, 2011, pp. 9–16 (2011).
[39] Y. Wang, T. Chen, P. Wang, C. Rohkohl, D. Comaniciu, Automatic Localization of Balloon Markers and Guidewire in Rotational Fluoroscopy with Application to 3D Stent Reconstruction, in: Computer Vision – ECCV 2012, Springer Berlin Heidelberg, 2012, pp. 428–441 (2012).
[40] R. Kandepu, L. Imsland, B. A. Foss, Constrained state estimation using the unscented kalman filter, 2008 Mediterranean Conference on Control and Automation - Conference Proceedings, MED'08 (2008) 1453–1458 (2008).
[41] K. Takashima, R. Shimomura, T. Kitou, H. Terada, K. Yoshinaka, K. Ikeuchi, Contact and friction between catheter and blood vessel, Tribology International 40 (2) (2007) 319–328 (feb 2007).
[42] M. Sanz-Lopez, J. Dequidt, E. Kerrien, C. Duriez, M.-O. Berger, S. Cotin, Testbed for assessing the accuracy of interventional radiology simulations, in: ISBMS - 6th International Symposium on Biomedical Simulation, LNCS, Springer, Strasbourg, France, 2014, pp. 155–159 (Oct. 2014).